Modeling Cardiac Function

With Particle Image Velocimetry

by

John Curtis Westerdale

A Dissertation Presented in Partial Fulfillment
of the Requirements for the Degree
Doctor of Philosophy

Approved March 2015 by the
Graduate Supervisory Committee:

Ronald Adrian, Chair
Marek Belohlavek
David Frakes
Steven Trimble
Kyle Squires

ARIZONA STATE UNIVERSITY

May 2015

ABSTRACT

The application of novel visualization and modeling methods to the study of cardiovascular disease is vital to the development of innovative diagnostic techniques, including those that may aid in the early detection and prevention of cardiovascular disorders. This dissertation focuses on the application of particle image velocimetry (PIV) to the study of intracardiac hemodynamics. This is accomplished primarily though the use of ultrasound based PIV, which allows for *in vivo* visualization of intracardiac flow without the requirement for optical access, as is required with traditional camera-based PIV methods.

The fundamentals of ultrasound PIV are introduced, including experimental methods for its implementation as well as a discussion on estimating and mitigating measurement error. Ultrasound PIV is then compared to optical PIV; this is a highly developed technique with proven accuracy; through rigorous examination it has become the "gold standard" of two-dimensional flow visualization. Results show good agreement between the two methods.

Using a mechanical left heart model, a multi-plane ultrasound PIV technique is introduced and applied to quantify a complex, three-dimensional flow that is analogous to the left intraventricular flow. Changes in ventricular flow dynamics due to the rotational orientation of mechanical heart valves are studied; the results demonstrate the importance of multi-plane imaging techniques when trying to assess the strongly three-dimensional intraventricular flow.

The potential use of ultrasound PIV as an early diagnosis technique is demonstrated through the development of a novel elasticity estimation technique. A

finite element analysis routine is couple with an ensemble Kalman filter to allow for the estimation of material elasticity using forcing and displacement data derived from PIV. Results demonstrate that it is possible to estimate elasticity using forcing data derived from a PIV vector field, provided vector density is sufficient.

To my parents, Norm and Donna,
for their loving support and encouragement.

ACKNOWLEDGEMENTS

I would like to extend my deepest appreciation to Dr. Marek Belohlavek for being an excellent mentor and for his tremendous support and guidance throughout my graduate career. I would also like to thank Dr. Michele Milano for inspiring me to pursue a graduate degree and Dr. Ronald Adrian for his guidance as my committee chair and the considerable impact his career has had on the research fields discussed within this dissertation. I would like to acknowledge and extend my gratitude to my committee members, Dr. Kyle Squires, Dr. Steven Trimble, and Dr. David Frakes. I would like to acknowledge the financial support from the Science Foundation of Arizona, Mayo Clinic, and Arizona State University. Finally, I am indebted to my family, friends, and the many people that I have worked with at ASU and at Mayo Clinic, including Dr. Eileen McMahon, Dr. Jeff Heys, and Robert Spade.

TABLE OF CONTENTS

Page

LIST OF TABLES

LIST OF FIGURES

Figure Page

Figure Page

Chapter 1

INTRODUCTION

According to a World Health Organization study published in 2012, the world's leading cause of death, claiming the lives of 7.4 million people that year, was ischemic heart disease. Stroke and hypertensive heart disease claimed the 2nd and 10th spots, respectively, with 6.7 and 1.1 million deaths in 2012 [1]. Cardiovascular related diseases remain the leading cause of death for Americans and the world's population. It is clear that the current methodology for diagnosing and treating cardiovascular disease is lacking.

Perhaps one of the primary issues leading to the prevalence of cardiovascular diseases is the failure of patients to receive preventative treatment when such treatment is still viable. Treatment of cardiovascular diseases often occurs after the onset of initial symptoms. As an example, valvular stenosis; in particular, aortic stenosis, which is often caused by calcification of the aortic valve, usually manifests as shortness of breath or dizziness [2]. However, treatment after the onset of symptoms can be rigorous and may require lifelong use of medication and drastic lifestyle changes. Depending on the severity of valvular disease, corrective surgery such as valvular replacement may be necessary. If an aortic stenosis is detected early, when the patient is asymptomatic, the prognosis is much more favorable and treatment will be primarily focused on minor lifestyle changes to improve health. Treatment of cardiovascular diseases is not a primary focus of this dissertation; instead, this often requires methods that are patient-specific and must be determined by a clinician. The primary focus of this research is on the diagnosis

of cardiovascular diseases, particularly diagnostic methods that could potentially prevent a patient from requiring invasive treatment.

Diagnosis techniques for heart diseases can be based on measurements of intracardiac hemodynamics, such as velocity or pressure; the structure of the myocardium; electrical conduction of the heart tissue; heart rhythm and rate; and cardiac output. In the design and development of diagnosis techniques, several considerations must be taken into account. Such techniques should be inexpensive, especially given the prevalence of heart disease among the under-privileged; they must also be accurate, repeatable and reliable; finally, they should be relatively simple for a clinician to implement. Magnetic Resonance Imaging (MRI), a diagnosis method that is considered to be particularly reliable, is prohibitively expensive for use in all but the most extreme circumstances. In contrast, Doppler ultrasound, although relatively inexpensive and reliable, is highly susceptible to operator error and examinations must be performed by experienced sonographers [3].

Perhaps one of the most important aspects in the development of diagnostic methods is the creation of early diagnosis techniques that allow for the detection of cardiovascular disease before treatment with medication or surgery is required. Early diagnosis techniques can allow a patient to make lifestyle changes, such as exercising regularly or implementing dietary changes, before their symptoms become more severe. Considering the early onset of cardiovascular diseases can result in pathophysiologies that are difficult to perceive, such as altered intraventricular flow, these techniques must be sensitive enough to detect such pathophysiologies before the patient is noticeably symptomatic. Baseline conditions can vary widely between patients based on overall

health, age, sex, and patient-specific physiology; thus, a diagnosis technique should also be adaptable for each patient.

Several recent technological advancements allow for the development of novel diagnosis techniques that would have previously been impossible. Flow visualization methods that allow for direct measurement of *in vivo* hemodynamics can be coupled with experimental models to create entirely new diagnostic techniques, an example being the tissue compliance estimation routine discussed in Chapter 5. By altering boundary conditions, such models can also be used to assess patient-specific dysfunction.

1.1 Background of Cardiovascular Modeling

Study of the cardiovascular system, and, more specifically, study of intracardiac flow, has throughout history been of paramount importance to the medical field. Perhaps the first detailed observations of the cardiovascular system come from the teachings of the Greek philosopher Aristotle, one of the first scholars to postulate the important role the heart plays in human physiology. However, the most incredible of these early studies of hemodynamic function is found in the research journals (dating from 1508-1509, and 1513) of Leonardo Da Vinci. Using what was believed to be a glass model of the left ventricle, he was the first to correctly predict, and accurately model, the occurrence of the ventricular vortex [2]. Da Vinci's genius extended to his research of arteries, vessels, capillaries, accurate conceptualization of cardiac function, and detailed studies of heart valve mechanics. He was perhaps the first to understand the open and closure dynamics of heart valves in response to a pulsatile flow generated during each heartbeat [4].

Confirmation of his early observations would take centuries and require technological advancements that would allow for quantification of cardiovascular function.

Cardiac flow visualization has its basis in technology created during the Second World War. Following the war these advancement were adapted for peace time use, thus resulting in the creation of rudimentary ultrasound imaging devices and breakthroughs in the understanding of nuclear magnetic resonance [5]. With the advent of phased-averaged magnetic imaging systems and echocardiography, which allow for non-invasive, *in vivo* testing, scientists were finally able to demonstrate the existence of energy-conserving intraventricular vortices; thus confirming Da Vinci's original hypothesis [4]. Within the last decade, methods allowing for direct in vivo visualization, and experimental methods such as computer-based numerical simulations and detailed *in vitro* studies have finally revealed the intricacies of cardiovascular hemodynamics.

1.2 Organization of this Dissertation

This dissertation is comprised of four distinct sections that offer incite into cardiac functioning, challenges of cardiac modeling and also an explanation of existing techniques. Chapters 3, 4, and 5 realted directly to the development of ultrasound PIV and novel diagnostic techniques; this is outlined in Figure 1.1.The primary focus of this dissertation is on the application of the PIV technique as a diagnostic tool; thus, a detailed analysis of the ultrasound PIV method is given along with examples of its implementation and potential to diagnose cardiac disorders. Descriptions of each section are provided below.

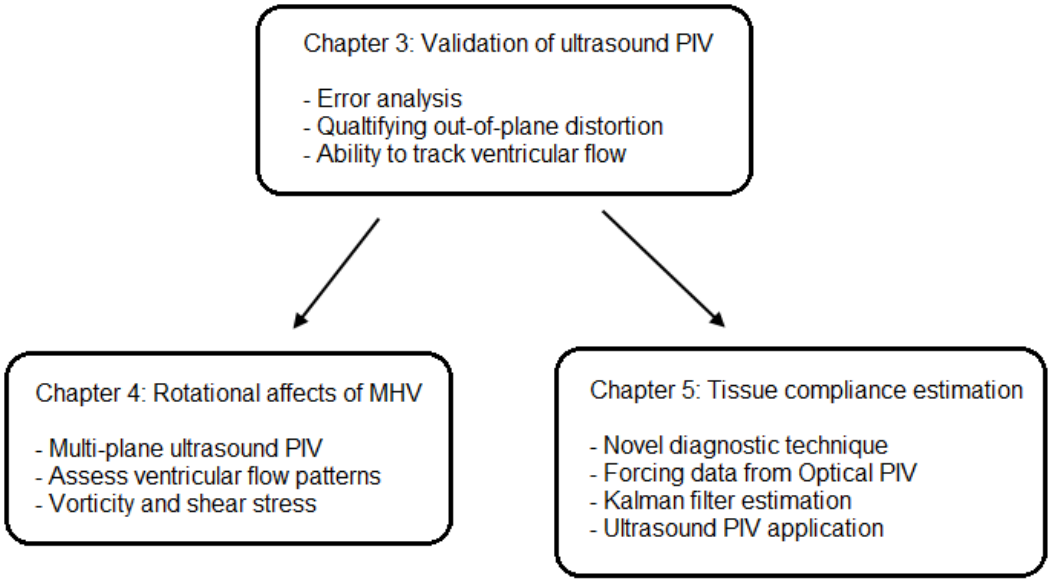

Figure 1.1 Dissertation outline showing the development and validation of ultrasound PIV as a clinical diagnostic tool

Chapter 2: Modeling of Intracardiac Hemodynamics. This section begins with a brief overview of cardiac functioning, including a detailed description of the cardiac cycle. Challenges associated with the modeling of cardiac functioning, including the irregular boundary conditions of the myocardium, are also discussed. Finally, an overview is provided for several modeling techniques, both computational and experimental, along with an analysis of intracardiac visualization techniques such as MRI and ultrasound PIV.

Chapter 3: Flow Velocity Vector Fields by Ultrasound Particle Imaging Velcimetry: In Vitro Comparison to Optical Flow Velocimetry. This section introduces the fundamentals of ultrasound PIV, including experimental methods for its implementation as well as a discussion regarding the level of error in measurements. Ultrasound PIV is then

compared to optical PIV; this is a highly developed and accurate technique that, through rigorous examination, has become the “gold standard” of two-dimensional flow visualization.

Chapter 4: Effects of Bileaflet Mechanical Mitral Valve Rotational Orientation on Left Ventricular Flow Conditions. This section demonstrates the application of multi-plane ultrasound PIV to quantify a complex, three dimensional flow that is analogous to the left intraventricular flow. Also of interest is the experimental use of a left heart model to approximate cardiac functioning and allow for in vitro testing.

Chapter 5: Elasticity Estimation Using Optical Particle Image Velocimetry Velocity Fields. This section extends the use of PIV as a diagnostic tool through its application in a novel elasticity estimation routine that could potentially be used to measure the compliance of the myocardium or heart valve leaflets.

Chapter 2

VISUALIZATION AND MODELING OF INTRACARDIAC HEMODYNAMICS

This chapter investigates the processes by which researchers are able to model, either through simulation or based on direct *in vivo* observation, the intracardiac flow. The primary focus of this dissertation will be on flow within the left ventricle (LV) and the transvalvular flow for the mitral and aortic valves, where the former is the 'inlet' and the latter being the 'outlet' of the LV. This selection is not arbitrary; the left heart is of extreme physiological importance considering its primary function is to pump oxygenated blood throughout the body [2]. Deviation from normal functioning of the left heart can, in many ways, be more debilitating when compared to similar pathophysiologies encountered in the right heart. Although not discussed, methods outlined within this chapter can be extended to the right ventricle and its valves (tricuspid and pulmonary valves), and also to the right and left atrium.

This chapter will provide an overview of widely used hemodynamic flow visualization techniques and modeling considerations. The primary focus will be on ultrasound-PIV (echo PIV) and MRI visualization techniques, both of which are leading methods in the research of intracardiac flow. Much work has been dedicated to both of the aforementioned methods and detailed explanations are readily available. Before delving into the techniques used for intracardiac hemodynamic modeling, a brief overview of cardiac function is given. Although often described in a mechanical sense as a pump, the heart is a tremendously complex biological system that presents many challenges when researchers attempt to study or model its function, particularly if the

heart is diseased. Understanding these challenges is paramount to determine the benefits and limitations of each method used to model or measure intracardiac flow.

2.1 Anatomy of the Heart

The function of the four-chambered heart is to pump oxygenated blood to cells throughout the body and then move deoxygenated blood back to the lungs. The cardiovascular system can be divided into the two separate circulatory systems: systemic circulation and pulmonary circulation. Systemic circulation carries oxygenated blood from the heart and into the body, and then transports deoxygenated back to the heart. Pulmonary circulation transports deoxygenated blood from the heart to the lungs and then carries oxygenated blood back to the heart [2].

The four chambers of the heart are: the left and right atria and the larger left and right ventricles. The function of the left and right atria is to allow continuous venous filling to occur, uninterrupted by the contraction of the ventricle. Unlike the ventricles there exists no valve at the inlet of the atria. The atrium prevents venous flow from being pulsatile; flow enters the atrium continuously, including when the atrium is being emptied into the ventricle. Atria are analogous to the priming mechanism of a mechanical pump system; where the ventricle is the actual pump mechanism and the volume of the ventricle corresponds to the displacement of the pump for each cycle. Because of this, both ventricles operate at higher pressures than the atria and are surrounded by a thicker myocardium. The left ventricle is responsible for pumping oxygenated blood into the aorta and throughout the body; this results in higher operating pressures than the right

ventricle, which is pumping deoxygenated blood through the pulmonary arteries directly to the lungs [2].

The heart also has four distinct valves that control flow directionality. The two atrioventricular (AV) valves: the mitral valve, positioned between the left atrium and ventricle; and the tricuspid valve, positioned between the right atrium and ventricle. Also, the two semilunar (SL) valves: the aortic valve, positioned between the left ventricle and aortic root; the pulmonary valve, positioned between the right ventricle and pulmonary artery. Each valve is comprised of two, three, and sometimes four leaflets that open and close due to pressure variations between the atrium and ventricle or ventricle and outflow tract [2].

The cardiac cycle describes the stages the heart undergoes from the initiation of a heart beat to the beginning of the subsequent heart beat. The cycle begins with a stage referred to as atrial systole, the atria contracts allowing blood to rush into the ventricle. During this stage as blood rushes through the mitral valve and into the LV, a vortex is generated from the inflow jet. The diastolic vortex, typically observed only in healthy hearts, is believed to aid in the closure of the mitral valve and also increase the overall cardiac efficiency [CITE]. The atrioventricular valves close during the second stage, isovolumic contraction, while the ventricle starts to contract while maintaining a constant volume. The third stage of the cardiac cycle is ventricular ejection, the semilunar valves open while the ventricles contract, pushing blood into the outflow tract. The fourth stage is isovolumic relaxation, the ventricle has stopped contracting and is now becoming relaxed, the semilunar valves close while the atrioventricular valves remain closed. The final stage is ventricular filling, the semilunar valves are closed while the atrioventricular

valves are open. Atrial systole and ventricular systole represents the moment when the atria and ventricles, respectively, are contracting. Atrial diastole and ventricular diastole represents the moment when the atria and ventricles, respectively, are relaxed. Due to the helical arrangement of the myocardium fibers around the ventricles, contraction of the ventricle occurs in a twisting manner. This helical arrangement of fibers also allows the ventricles to convert part of its kinetic energy during contraction into potential energy via elastic recoil to generate a pressure gradient that aids in the suction of blood into the ventricle during the isovolumic relaxation stage. This event is known as 'untwisting' and can be difficult to replicate in cardiac models. [2, 6]

2.2 Review of Methods for Intracardiac Flow Visualization

Capturing in vivo hemodynamic measurements can be difficult. Researchers must contend with the many limitations of current visualization methods; this includes limitations related to temporal and spatial resolution, but special considerations must also include patient comfort and the invasiveness of the procedure. Scan time, breath holding, and the use of contrast agents all contribute to patient discomfort. Another consideration is the difficulty of obtaining pertinent measurements. As an example, ultrasound measurements of the peak transaortic velocity, used to diagnose aortic stenosis, may require imaging planes that are impossible to access external to the body; thus, transesophageal echocardiography may be required.

Common intracardiac visualization techniques: MRI, color Doppler, and ultrasound PIV are discussed in the next sections; however, a more detailed discussion has been performed by Sengupta et al [3].

2.2.1 Cardiac Magnetic Resonance Imaging

Velocity encoded cardiac magnetic resonance (CMR) phase-contrast imaging allows for multidirectional measurement of intracardiac hemodynamics. Real time two dimensional data acquisition is possible, however, averaging between multiple heart cycles using electrocardiogram gating allows for the acquisition of fully three dimensional velocity data, with high resolution in each dimension, over a complete cardiac cycle. The interrogation window can be large enough to encompass the entire heart. Both spatial and temporal resolutions are dependent upon interrogation window size. High spatial resolution can be acquired within a 3mm cube with temporal resolution of 50 ms. Limitations of this method include the time required to acquire data, this may exceed 20 minutes depending on the desired resolution; poor resolution for real time data; and also the high cost of the MRI equipment [3].

2.2.2 Echocardiography

Various ultrasound-based methods can be employed to measure intracardiac velocity; these include Doppler ultrasound, color flow Doppler, vector flow mapping (VFM), and ultrasound PIV. Only the latter two will be discussed due to their ability to resolve two dimensional velocity vector fields. VFM utilizes data derived from color flow Doppler, which typically only resolves one dimensional axial velocity within an

ultrasound beam, to calculate the out-of-beam radial velocity component. This is accomplished numerically by assuming the radial flow is comprised of laminar flow with a vortical component that has zero mean. The out-of-beam velocity is then estimated by assuming the flow satisfies the continuity equation; depending on the complexity of the flow, the aforementioned assumptions necessary for the calculation of the radial velocity may be incorrect [3].

Ultrasound PIV utilizes the principles of PIV to obtain a two dimensional velocity vector field. Two dimensional B-mode ultrasound scans are acquired and offline tracking of contrast agents seeded within a flow is performed. The spatial and temporal resolution is highly dependent on the size of the interrogation region. Temporal resolution can reach 4 ms with a spatial resolution of 4 mm; however, much lower resolution can be expected if the imaging region encompasses the ventricles. Three dimensional data is not readily available unless multi-plane acquisition methods are used, although this has not been thoroughly studied for in vivo applications. The primary benefit to ultrasound techniques is the relatively low cost of the equipment and high temporal resolution, particularly when compared to MRI [3,6]; however, there is a tradeoff with spatial resolution and the ability to image in 3D.

2.3 Considerations of Cardiac Modeling

Numerous techniques exist for modeling the heart. A summary of popular computational fluid dynamic (CFD) methods, including a discussion on the incorporation of ultrasound PIV data to enhance modeling, is provided in Borazjani, Westerdale et al [6]. Of particular consideration when modeling cardiac function is the development of

boundary conditions that correctly simulate the myocardium. This can be especially difficult as the myocardium expands and contracts, in a twisting manner, with each heart beat. Furthermore, geometry of the heart is irregular and specific to each individual; also, the myocardium has nonhomegeneous elasticity and thickness. Visualization techniques that delineate the cardiac structure can be used to derive patient-specific boundary conditions and visualization techniques that capture the intracardiac flow can be coupled with models to improve the ability of the model to correctly simulate cardiac hemodynamics.

Modeling of the cardiovascular system is often performed to aid in both the treatment and detection of cardiac diseases and their subsequent pathophysiologies. Replicating a particular disease can be extremely difficult; a cardiac infarction, for instance, can alter the twisting and untwisting motion of the myocardium and also change the electrical activity of the heart, leading to an irregular heartbeat. Ventricular hypertrophy, the thickening of the ventricular walls, can affect the ventricle globally or regionally, and the level of severity or extent of cardiac remodeling that occurs will be specific to each patient. Thus, each disease that is modeled often requires revised boundary conditions.

Chapter 3

FLOW VELOCITY VECOTR FIELDS BY ULTRASOUND PARTICLE IMAGING VELOCIMETRY: IN VITRO COMPARISON TO OPTICAL FLOW VELOCIMETRY

The objective of this study is to perform an in vitro study to assess the precision and accuracy of particle imaging velocimetry (PIV) data acquired using a portable ultrasound system via comparison with optical-PIV. The performance of ultrasound-PIV, where data are collected using a GE Vivid *i* portable system, is compared with a LaVision optical-PIV system on a benchmark problem involving a vortical flow with a significant out-of-plane velocity component. Optical-PIV is capable of stereo image acquisition, thus measuring out-of-plane velocity components. This allowed us to quantify the accuracy of ultrasound-PIV, which is limited to in-plane acquisition. The system performance is assessed by considering the instantaneous velocity fields, without extracting velocity profiles by spatial averaging. Within the two-dimensional (2D) correlation window, using 7 time-averaged frames, the vector fields were found to have a correlation of .867 in the direction along the ultrasound beam and .738 in the perpendicular direction. Out-of-plane motion greater than 20% of the in-plane vector magnitude was found to increase the standard deviation by 11% for the vectors parallel to the ultrasound beam direction and 8.6% for the vectors perpendicular to the beam. The results show a close correlation and agreement of individual velocity vectors generated by ultrasound-PIV and compared to optical-PIV. Most of the measurement distortions occurred due to out-of-plane velocity components.

3.1 Introduction

Particle imaging velocimetry (PIV) is a velocity field measurement method that works by calculating the velocity of neutrally buoyant tracer particles seeded within the flow. Ultrasound-PIV, originally described by Shandas et al. [7, 8], is well suited for characterization of intracavitary blood flow velocity vectors by using microbubbles as ultrasound contrast agents (UCA) captured in sequences of 2D brightness (B)-mode ultrasound scans [9, 10]. In essence, ultrasound-PIV represents a novel use of existing engineering principles of optical-PIV applied to brightness signals generated by microbubbles and tracked in sequential ultrasound images by software. To obtain local flow velocity vectors and velocity maps, the software calculates displacements of UCA over a given time interval, which is typically determined by the actual frame rate.

A measure of the accuracy of ultrasound-PIV measurements is essential for advancing the analyses of intracardiac flow patterns from rather descriptive and qualitative studies to quantitative blood flow analyses. Previous studies explored the versatility of the ultrasound-PIV method by investigating the range of measurable flow velocities, providing a quantitative analysis of spatially averaged velocity fields for a laminar flow, and offering a qualitative analysis of a 2D velocity vector map for a rotating flow [7, 8].

Using an in vitro setup, the purpose of this study was to initially assess the suitability of ultrasound-PIV data produced from scan-converted serial images generated by a commercially available, portable, and relatively inexpensive ultrasound imaging system. This was accomplished by quantitative analysis of 2D velocity fields generated from ultrasound-PIV scans of flow with both in and out-of-plane components. Precision

(correlation) and accuracy (bias) of local vector velocities generated by ultrasound-PIV was compared to optical-PIV used as the reference.

3.2 Materials and Methods

3.2.1 Optical Particle Image Velocimetry

The reference optical-PIV measurements in this study were obtained using a LaVision Flow Master acquisition system and DaVis software (LaVision GmbH, Göttingen, Germany). The system consists of two charge-coupled device (CCD) Imager Intense cameras that are synchronized with a 700 mJ argon-ion laser, which acts as the 'flash' for the images. The laser light reflected by tracer particles provides contrast from background noise.

The actual velocity is measured by tracking particle displacement between two high-speed images recorded by the camera with a time step dependent upon flow velocity and window size (3 ms for the experiment presented here). To achieve this, the laser generates a double pulse and the CCD camera records the two corresponding images from two separate exposures. The optical-PIV system pauses for an increased time step (17.6 ms) until taking an additional image pair. The optical-PIV system used in this experiment acquires stereo data. Two cameras are situated at different viewing directions to record both the 2D in-plane components and the out-of-plane velocity components. The "angular displacement" system is the standard configuration for the cameras [11]. The actual visualization area, both in-plane and out-of-plane, is determined by the width of the laser sheet (approximately 2 mm at 75% intensity).

The images have been processed using DaVis software, version 7.2.2.80. Briefly, a fast Fourier transform cross-correlation technique is applied and images are processed using an iterative scheme with multiple passes of decreasing interrogation window size. For each iteration, the corresponding window size and weight, percent overlap, and number of passes can be selected. The determination of particle displacement between image pairs leads to the calculation of flow velocity.

3.2.2 Ultrasound Particle Image Velocimetry

The implementation of ultrasound-PIV is analogous to optical-PIV; the most significant difference is the image capturing technique. While optical-PIV requires visual access to the flow, ultrasound-PIV uses high-frequency sound transmission to detect the position of UCA dispersed within the flow. A Vivid *i* (GE Healthcare, Milwaukee, WI) portable ultrasound imaging system, was used in our study to produce B-mode 2D sector scans. The scans were obtained with a 3S-RS phased-array transducer operating at 3.6 MHz frequency at a depth of 17cm with a mechanical index (MI) of 1.1. The 2D transducer imaging axis was aligned with the optical-PIV laser sheet (**Figure 1**). The DICOM video images exported by the Vivid *I* were scan converted and the resulting images have square pixels of 0.435 mm in size.

3.2.3 Ultrasound Contrast Agent

Optison (GE Healthcare) was used in this study. In clinical applications, UCA is administered in a large enough quantity so as to produce maximum backscatter to delineate cardiac structures. However, when performing ultrasound-PIV, a significantly lower concentration is used so that individual particles can be tracked between frames

and their overlap within the interrogation (image sampling) window is minimized. The UCA concentration has been shown to significantly affect the quality of ultrasound-PIV results [8]. Because cross-correlation analysis is in the core of tracking particle motion between frames, we used cross-correlation index (CCI) [8] as the measure of optimal UCA concentration. CCI is defined as follows:

$$CCI = \sum_{x=N_0}^{N_1} \left(\frac{f(x) F_{\max}}{f_{\max} F(x)} \right) \tag{3.1}$$

where $F(x) = \frac{1}{\sqrt{2\pi}\sigma} \exp\left(\frac{(x-\mu)^2}{2\sigma^2} \right)$ is a Gaussian fitting function, $f(x)$ is the cross-correlation peak fitting function, x is the total number of pixels within the interrogation window, σ is the standard deviation of the Gaussian fitting function, and μ is the interrogation window size. The minimum interrogation window size is determined using the one quarter rule [12]. The rule, used for both optical- and ultrasound-PIV, states that particle displacement (in pixels) should be no greater than one quarter of the minimum interrogation window size [8]. Particles with a greater velocity will move out of the interrogation window, thereby necessitating a larger window size. Acceptable values for the CCI are within the range from 0.2 to 0.55 [8].

3.2.4 Experimental Apparatus

In order to investigate the correlation between vector maps generated by optical-PIV and ultrasound-PIV, a setup (**Figure 3.1**) was constructed so that both PIV analyses could be performed concurrently on a water jet injected into a water-filled chamber. The central

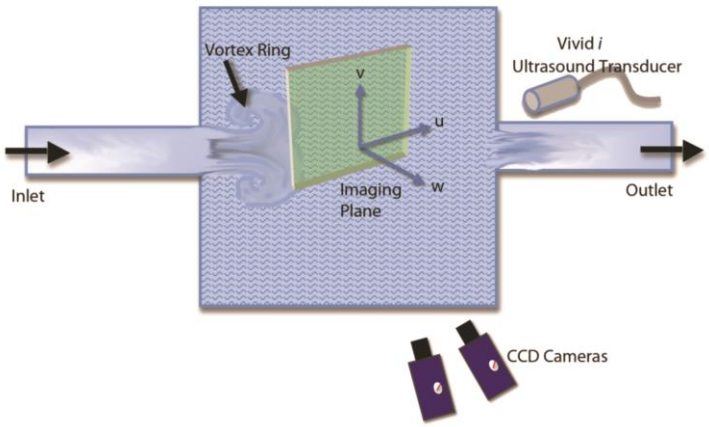

Figure 3.1 Experimental configuration. Three mutually perpendicular axes defined orientation in three dimensions as follows: u-direction was the direction of ultrasound transducer imaging axis, w-direction was perpendicular to the u-direction and the u-w plane was parallel with the fluid surface; v-direction and u-v plane were perpendicular to the u-w plane.

chamber, where imaging and ultrasound data are collected, is a closed, 15.4 cm cube manufactured using 1.2 cm thick transparent acrylic. The particular acrylic was selected based on the level of transparency and its distortion-free surface, making it ideal for optical-PIV measurements. There is a certain level of ultrasound attenuation as a result of the acrylic; however, it is not the goal of this study to investigate a scenario where attenuation is minimized, we instead investigate a scenario more similar to a clinical setting where attenuation is prevalent. The setup is a closed system whereby the inlet is connected to a pump submerged in a reservoir (at zero head with respect to the centerline

of the chamber) and the outlet vents directly into the reservoir. The inlet and outlet sections are both acrylic tubes 70 cm in length with a square cross-sectional area and inner diameter of 2.2 cm. This corresponds to the typical mitral valve annulus diameter of 2.1 to 2.7 cm [13]. The length and square cross-sectional area of the inlet tube was chosen to reduce the amount of 'swirl' within the flow. The jet is generated by a 20W, centrifugal pump which is triggered for 200 ms. The size of each vortex ring is dependent upon the flow volume, Reynolds number, orifice diameter, and ejection time [13]. The duration of each pump pulse was specifically chosen based on a series of trials so as to generate a single vortex ring with no shedding while maintaining a laminar flow. The Reynolds number for the flow characterized by the inlet tube diameter was approximately 1000, this ensures no turbulent effects are present. Thus, considering the flow is laminar, swirl is eliminated, and a precise triggering system employed, the jet pulses are fully repeatable. This allowed ultrasound-PIV and optical-PIV to be performed on separate occasions, which was necessary because the maximum imaging frequency of the optical-PIV was 2.5 frames/sec, whereas the frame rate of the ultrasound machine under the given conditions was 60 frames/sec. To compensate for this difference, a triggering system was designed so that the optical-PIV system would commence imaging following a given delay after the pump was activated. The initial delay was chosen so that imaging began once the jet entered the chamber. The triggering system, coupled with the repeatability of the flow, allowed us to collect precisely delayed optical-PIV measurements and assemble them to a time sequence that matched ultrasound-PIV measurements.

The tested peak flow velocity was 30 cm/s. The set temporal resolution of the Vivid-*i* machine (ie, 60 frames/sec) was adequate for this peak velocity and was supported by the serial DICOM output. The dimension of each vortex ring (one portion of the double vortex ring structure) was approximately 2 cm in the u- and v-directions.

We assessed precision by the Pearson's linear correlation and accuracy by the Bland/Altman methods, including the effects of outliers, measurement scale, and bias [14, 15].

3.2.5 Ultrasound-PIV Analysis

Optison, mixed in the original vial as instructed in the packaging, was injected in an amount of 0.5 mL into the tank and the pump was run for approximately 10 seconds to disperse the microbubbles evenly within the flow system. The initial UCA concentration was estimated at $2.3 \pm 2 \times 10^7$ microbubbles/mL. However, a significant number of microbubbles was destroyed by the ultrasound beam, collision with the pump or other surfaces, and diffusion. To develop a range for determining the appropriate concentration, two sets of data were collected at 30 sec, 60 sec, and 90 sec after the initial injection of Optison, where each time step corresponds to a decrease in concentration due to particle destruction. The total time to conduct each experiment was approximately 10s after the water pump was activated. The maximum CCI of 0.34, found 30 sec after the initial injection, was within the range of acceptable values; data corresponding to this CCI was used for the PIV analysis.

A particle intensity normalization was applied to the scan converted image to enhance the contrast between individual particles and background noise. Raw data collected from the left and right cameras of the optical-PIV system and raw data from the ultrasound scan are shown in **Figure 3.2**. The data was processed by the DaVis software using the iterative cross-correlation technique with decreasing interrogation window size. The maximum window size was 128 × 128 pixels with 50% overlap with adjacent interrogation windows and 2 passes of the processing , and the minimum window size was 32 × 32 pixels with 75% overlap and 3 passes. Approximately 16 particles were evident per interrogation window. Weighting factors were not applied to either window size. Vectors with magnitude exceeding two times the root-mean-square magnitude of neighboring vectors were automatically labeled as outliers and eliminated.

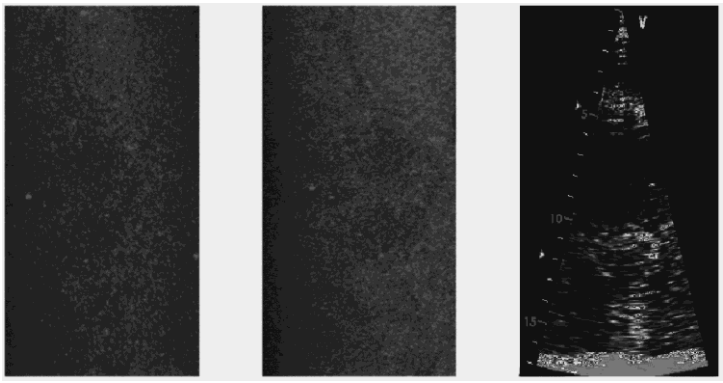

Figure 3.2 Raw data for the left camera of optical PIV (left), right camera of optical-PIV (middle), and the DICOM ultrasound image.

3.2.6 Optical-PIV Analysis

The optical data was processed analogously to the echo data, with the primary difference being a higher visible particle density than the ultrasound data that allowed the use of a maximum window size of 64 × 64 pixels with 25% overlap and 2 passes, and a minimum window size of 16 ×16 pixels with 50% overlap and 2 passes. There were

approximately 20 particles per interrogation window. Considering that interrogation window size affects spatial resolution, and a smaller interrogation window was used when processing the optical data, the echo results were spatially interpolated to match the vector density provided by optical-PIV. A smaller interrogation window allowed for more detailed optical-PIV vector fields and more incite into the accuracy lost by the limited resolution of the ultrasound scan.

The correlation window for the optical and ultrasound PIV velocity fields was 12.7 mm along the u-direction and 38.4 mm in the v-direction. The vector density was 1.144 vectors per mm^2 with a total vector density of 558 vectors. **Figure 3.3** shows the location of the correlation window as indicated by a translucent red square overlay on the echo and optical-PIV velocity fields.

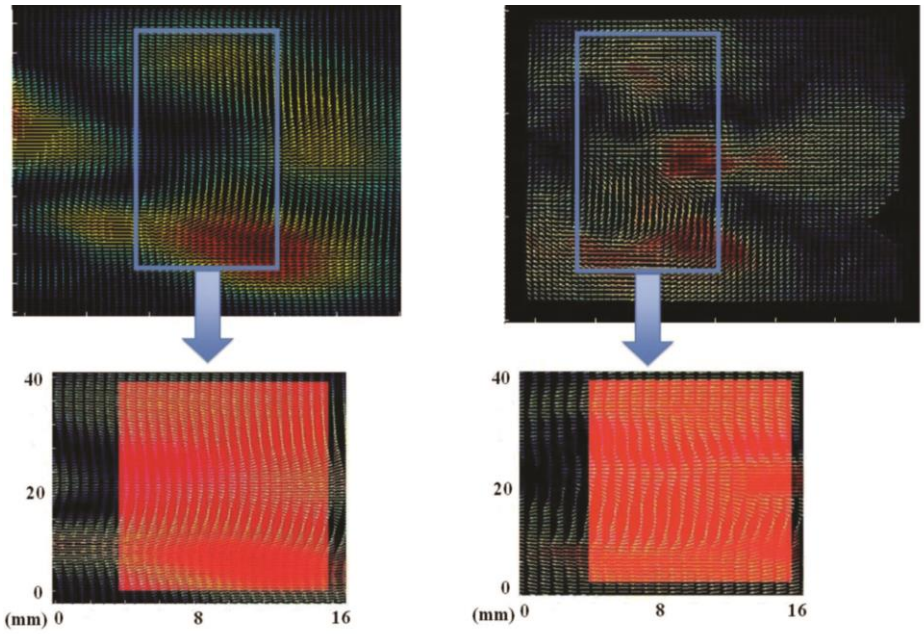

Figure 3.3 The red overlay indicates the location of the correlation window in relation to the velocity field for ultrasound-PIV (left) and optical-PIV (right).

3.3 Results

To minimize the noise in the ultrasound-PIV measurements, a moving average time filter was applied to the ultrasound-PIV velocity fields. The filter was also applied to the optical-PIV data to ensure identical velocity fields are compared, i.e. 3 averaged ultrasound-PIV data sets will have the same characteristics as 3 averaged optical-PIV data sets. This allows us to study the effects of a time average filter on noise in ultrasound measurements without considering error introduced by averaging flow characteristics. In this particular instance the flow remains virtually steady throughout the averaging cycle and the frame rate is sufficiently high so that only minimal error is introduced via the time averaging filter; however, this may not be the case in other applications. **Figure 3.4** shows the relation between the number of frames averaged and the resulting correlation between the averaged echo and optical velocity fields. The correlation coefficient increased with increasing number of frames averaged and reached the peak value of 0.802 with 7 frames averaged. The correlation factor was found to decrease when more than 8 frames were averaged. This is because the vortex ring gradually moves beyond the laser sheet and out of the field-of-view for optical-PIV.

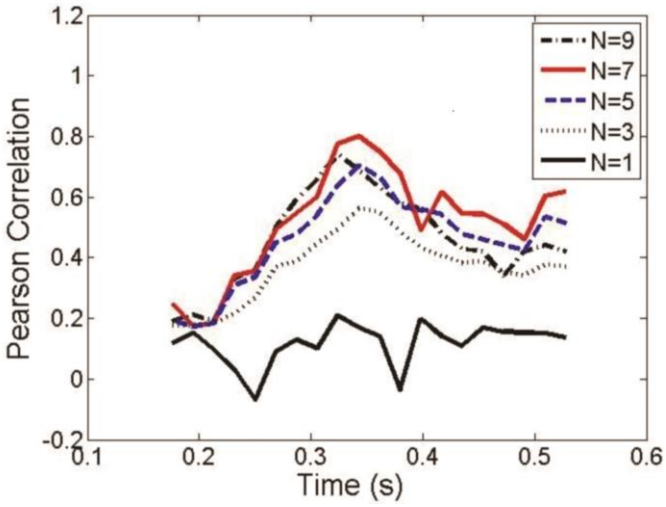

Figure 3.4 Plot of the number of averaged frames (N) used in filter versus the linear correlation coefficient for echo and optical-PIV over time. The maximum correlation was found at N = 7.

Within the correlation window, using 7 averaged frames, the ultrasound and optical velocity fields were found to have a correlation of 0.867 in the u-direction and 0.738 in the v-direction. The identity plot for the u-direction (**Figure 3.5a**) and v-direction (**Figure 3.5b**) show minimal visible bias in the data; the equation for the linear regression line further confirms this fact, where the u-direction is given by y=.9564x+.0201 and the v-direction is given by .9804x+.0219. When considering both the u and v directions, the correlation of vector magnitudes of the velocity fields was 0.802. The average error in the u-direction (along the ultrasound beam) was 5% less than the average error in the v-direction (perpendicular to the ultrasound beam). This discrepancy is indicative of the variations in ultrasound resolution in the axial (along the beam) and perpendicular directions. Perpendicular resolution is affected by factors such as beam width and interpolation due to the scan conversion process, where as axial resolution is a function of frequency [8].

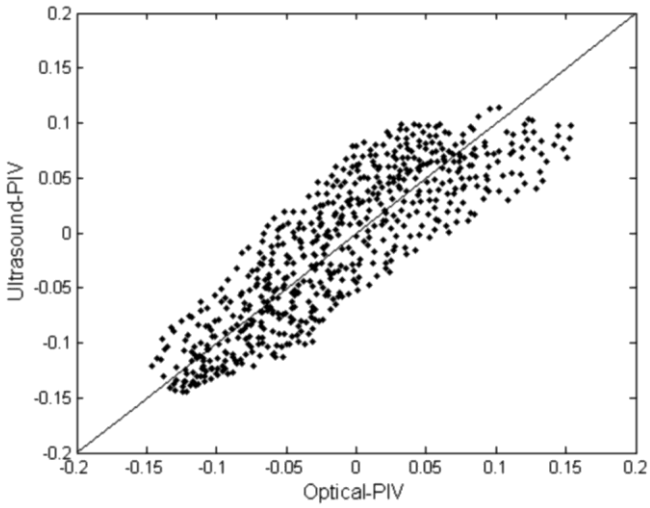
Ultrasound-PIV
Optical-PIV
0.2
0.15
0.1
0.05
0
-0.05
-0.1
-0.15
-0.2

(a)

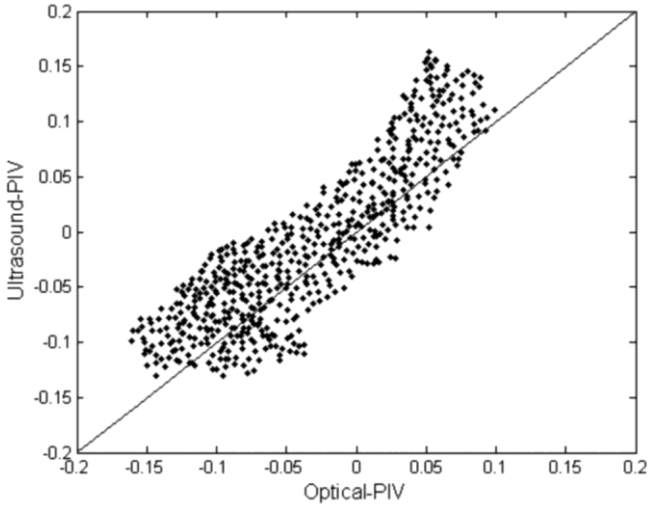
Ultrasound-PIV
Optical-PIV
0.2
0.15
0.1
0.05
0
-0.05
-0.1
-0.15
-0.2

(b)

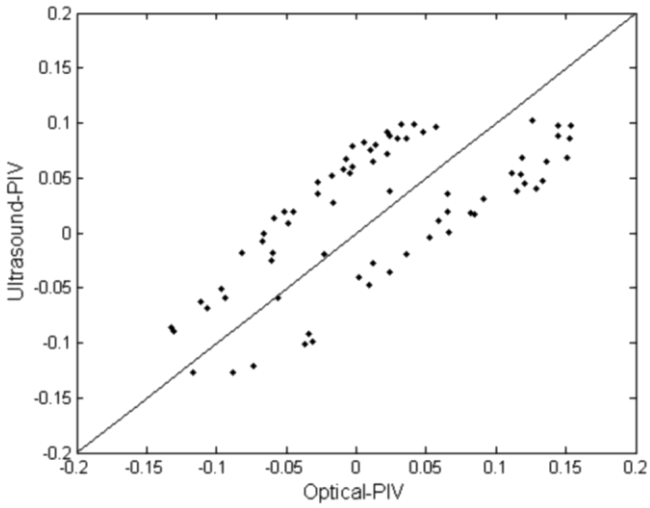

(c)

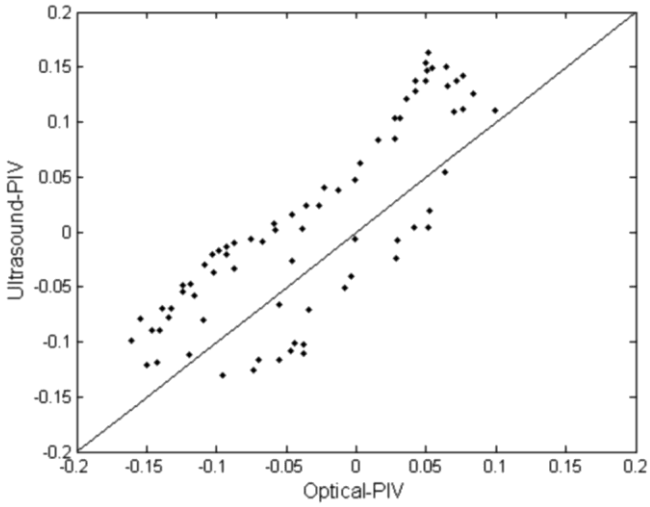

(d)

Figure 3.5 Identity plot of optical-PIV versus ultrasound-PIV velocities for (a) u-direction and (b) v-direction at a time of .34 seconds, corresponding to the maximum correlation coefficient. In addition, data points where out-of-plane motion is greater than 20% of the in-plane motion are plotted for (c) u-direction and (d) v-direction. More distortion is found in v-direction (perpendicular to ultrasound beam) than in u-direction.

Along the u-direction, 86% of the vectors have less than 20% error between echo and optical PIV, and along the v-direction, 74% of the vectors have less than 20% error. A

significant portion of the error greater than 20% is caused by the inability of ultrasound-PIV to track particles that move out-of-plane, as shown in **Figure 5c** and **5d**, where only vectors with an out-of-plane component greater than 20% of the in-plane vector magnitude are plotted. These vectors are found to congregate in regions with the highest level of error, corroborating the idea that a significant part of the flow velocity error in ultrasound-PIV comes from out-of-plane movement of the tracer particles. This idea is furthered when considering the Bland Altman plots in **Figures 3.6a** and 3.**6b;** the standard deviation decreases by 11% for the u-direction vectors and 8.6% for the v-direction vectors when points with high out-of-plane motion are ignored, as illustrated in **Figures 3.6c** and **3.6d**, respectively.

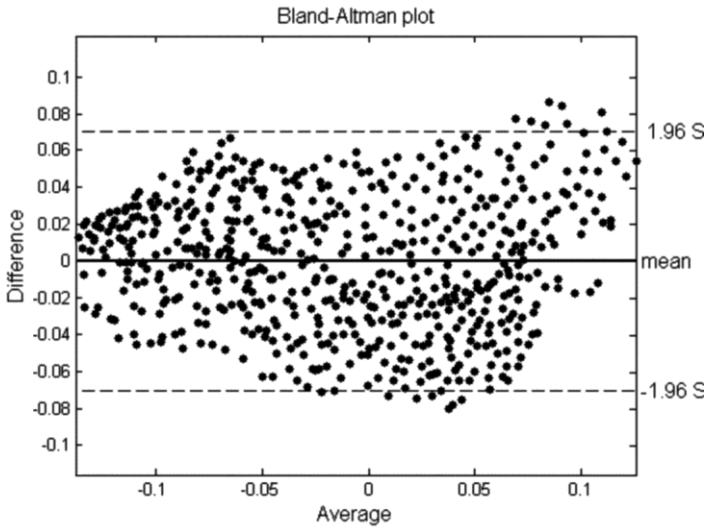

(a)

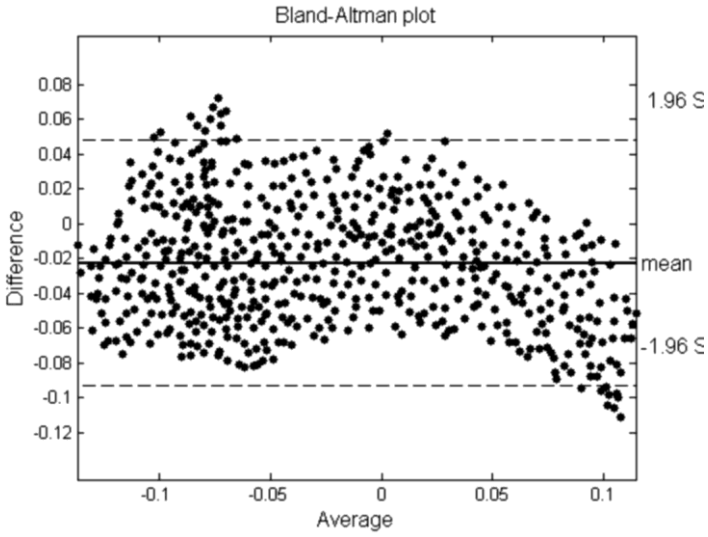
Bland-Altman plot
0.08
0.06
0.04
0.02
0
-0.02
-0.04
-0.06
-0.08
-0.1
-0.12
Difference
1.96 S
mean
-1.96 S
-0.1
-0.05
0
0.05
0.1
Average

(b)

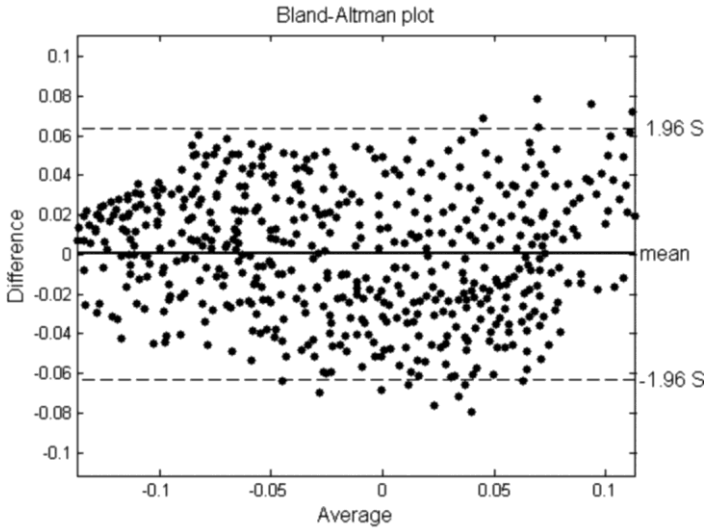
Bland-Altman plot
0.1
0.08
0.06
0.04
0.02
0
-0.02
-0.04
-0.06
-0.08
-0.1
Difference
1.96 S
mean
-1.96 S
-0.1
-0.05
0
0.05
0.1
Average

(c)

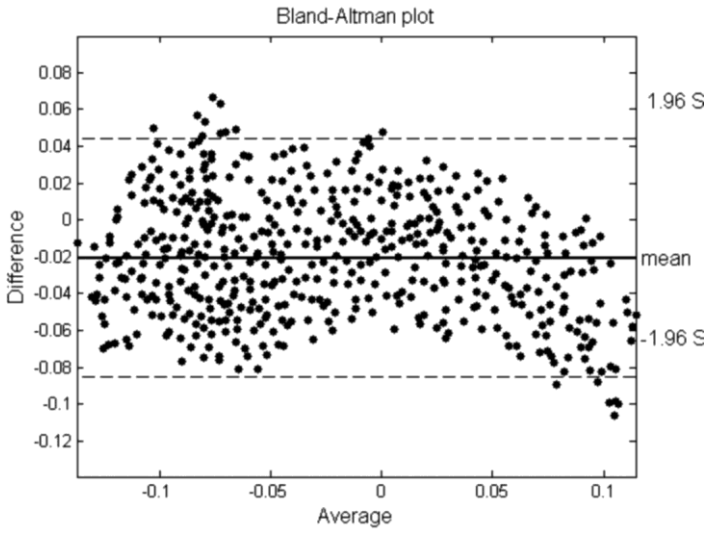

(d)

Figure 3.6 Bland Altman plots of optical-PIV versus ultrasound-PIV velocities for (a) u-direction, SD = 0.0365m/s and (b) v-direction, SD = 0.0351m/s. The corresponding plots where data points corresponding to out-of-plane motion greater than 20% of the in-plane motion are deleted for (c) u-direction, SD = 0.0324m/s (d) v-direction, SD = 0.0321m/s. The 95% confidence intervals are indicated by ±1.96 SD.

3.4 Discussion

The primary finding of this study is that ultrasound-PIV measurements of 2D velocity fields obtained for in-plane components of a three dimensional flow strongly correlate (Figures 3.5a, 3.5b) and closely agree (Figures 3.6a, 3.6b) with the corresponding local velocities measured by optical-PIV. Expectably, out-of-plane motion of flow affected both the correlation (Figures 3.5c and 3.5d) and agreement (Figures 3.6c, 3.6d). But we deem the overall precision and accuracy of ultrasound-PIV, using measurements obtained from a widely available, portable system, remains suitable for the tested flow velocities and the method could be extended to clinical applications.

Analysis of blood flow patterns inside the cardiovascular system conveys important information about functioning [16] and health status [17] of the heart. The ability to visualize and quantitatively evaluate blood flow patterns are important prerequisites for early diagnosis in cardiology [18]. Conventional Doppler ultrasound imaging provides quantitative data about blood flow velocities and pressure gradients [19, 20], but this method is angle-dependent, one-dimensional, and limited in detecting flow alterations in early stages of cardiac disease [13,21]. Garcia et al. [22] reported successful reconstruction of 2D intraventricular flow velocity maps by digital processing of color-Doppler velocities in combination with LV wall positions throughout the cardiac cycle. However, further validation of this method will be needed to show clinical utility. Magnetic resonance phase contrast velocity mapping, which is another imaging alternative for analysis of intracardiac flow, is burdened by high cost, has limited temporal resolution when compared to Doppler, and can lead to patient discomfort [23-25]. Considering these limitations, the technique is unlikely to be used widely in a clinical setting and, despite spatial resolution superior to ultrasound-PIV, the limited temporal resolution can restrict the imaging of heavily time dependent flows.

Ultrasound-PIV, with high temporal resolution and relatively low cost (particularly if conducted using readily available ultrasound equipment), offers several benefits over previous visualization techniques that may make it suitable for future clinical use. Advances in imaging techniques for mapping flow patterns with ultrasound-PIV [9,10,16] have enabled noninvasive and potentially broadly usable assessment of intracardiac flow patterns and fluid transport efficiency. Hong et al. [9] used ultrasound-PIV to analyze intraventricular blood flow in hearts of normal subjects and patients with

systolic dysfunction and demonstrated that ultrasound-PIV and depiction and vorticity analysis of intracardiac blood swirls could serve as a novel approach to qualitatively and quantitatively assess intraventricular flow structure. Gharib et al. [26] characterized optimal intracardiac hemodynamic conditions for diastolic vortex formation by the vortex formation time parameter and showed in a clinical study that vortex formation can be an index of cardiac health. We have also shown intracardiac vortex formation in the context of left ventricular function [27] and documented alterations of intraventricular vortices during asynchronous isovolumic phases of the cardiac cycle [10]. Moreover, we demonstrated that increased left ventricular pressure loading impairs diastolic vortex formation [16] and increases required transmitral flow forces [28].

Investigators in Shandas' group optimized ultrasound-PIV by microbubble backscatter modeling [29] and initially experimentally validated the method [7, 25]. The present study validates ultrasound-PIV in vitro against optical-PIV in a setting simulating diastolic vortex ring formation and demonstrates the ability of ultrasound-PIV to precisely and accurately assess local flow velocities. In this way, the presented work contributes to more extensive validation, further refinement and, ultimately, clinical implementation of the echo-PIV method.

3.4.1 Limitations

In the current study, flow velocities tested are relatively low flow velocities in comparison to the left ventricular diastolic filling flow and diastolic vortex formation [16]. Development of a more advanced flow model is anticipated to provide higher range of flow rates and options for testing various complex flow patterns. Higher temporal

resolution and, thus, frame rates in the order of hundreds of frames/sec, will be demanded by the new model. The Vivid-*i* system including its pulser/receiver hardware is miniaturized but its diagnostic performance is similar to high-end systems such as Vivid 7 or Vivid E9 (communication with GE Healthcare). However, full featured systems typically have faster processing hardware and software; thus if frame rates in the order of hundreds of frames/sec will be required, a high-end ultrasound system will be considered for echo-PIV to assure a sufficient reserve in temporal resolution.

The displacement of particles between consecutive frames is dependent upon the flow velocity. Referring to the one quarter rule [12], which dictates that particle displacement (in pixels) should be no greater than one quarter of the minimum interrogation window size [8], it is possible to estimate the frame rate for a desired interrogation window resolution at a given velocity. For instance, if a given velocity corresponds to a 16 pixel displacement between frames, then the minimum window size is 64x64 pixels; however, if a 32x32 pixel interrogation window is desired, then the frame rate will need to be doubled. If a time filter is to be used to minimize noise in ultrasound data, than a much higher frame rate will be required based on the level of filtering necessary.

The ideal situation for ultrasound-PIV data processing would be to use radiofrequency signals. The next best option would be saving the data as DICOM-raw files and perform ultrasound-PIV analysis prior to scan-conversion to minimize distortion of microbubbles by interpolation and smoothing typically used in the scan-conversion process. Kim et al. [7] demonstrated that such distortion can negatively impact flow analysis, as indicated by spurious velocity vectors along the top and bottom edges of the scan-converted images. To minimize the effect of distortion along the edges, here we chose the depth and width

of the ultrasound scan so that the area of interest (position of the vortex rings) was within the center of the sector image. Overall, our approach of using standard DICOM output and scan-converted images simulated a simple, clinically feasible workflow, and the results confirmed precision and accuracy of the measurements.

3.5 Conclusion

In the given experiment, 2D velocity vector fields obtained by a clinically available, portable ultrasound machine coupled with DaVis PIV processing software are shown to be highly correlated and in a close agreement with those generated by optical-PIV, a technique well established as a standard for flow visualization [12,13,25]. The vortex ring imaged in this experiment contained a significant out-of-plane component, and much of the measurement error is shown to occur from the inability of 2D ultrasound to measure out-of-plane flow motion. Additional measurement error can be attributed to distortion due to the scan conversion process of ultrasound data. Given sufficient ultrasound frame rate, a time filter can be applied to minimize noisy data. Using 7 averaged frames on a flow with 30cm/s peak velocity measured at 60fps, the correlation was found to be .867 in the direction along the ultrasound beam and .738 in the perpendicular direction. Thus, ultrasound-PIV is precise and accurate in the measured velocity range with most limitations related to 2D scanning of flow, which naturally contains velocity vectors in multiple directions.

Chapter 4

EFFECTS OF BILEAFLET MECHANICAL MITRAL VALVE ROTATIONAL ORIENTATION ON LEFT VENTRICULAR FLOW CONDITIONS

We studied left ventricular flow patterns for a range of rotational orientations of a bileaflet mechanical heart valve (MHV) implanted in the mitral position of an elastic, ellipsoidal model of a beating left ventricle (LV). The valve was rotated through 3 angular positions (0, 45, and 90 degrees) about the LV long axis. Ultrasound scans of the elastic LV were obtained in four apical 2D imaging projections, each with 45 degrees of separation. Particle imaging velocimetry was performed during the diastolic period to quantify the in-plane velocity field obtained by computer tracking of diluted microbubbles in the acquired ultrasound projections. The resulting velocity field, vorticity, and shear stresses were statistically significantly altered by angular positioning of the mechanical valve, although the results did not show any specific trend with the valve angular position and were highly dependent on the orientation of the imaging plane with respect to the valve. We conclude that bileaflet MHV orientation influences hemodynamics of LV filling. However, determination of ‘optimal’ valve orientation cannot be made without measurement techniques that account for the highly 3-dimensional intraventricular flow.

4.1 Introduction

The use of MHVs is widely accepted. However, the blood flow patterns following MHV implantation are altered compared to those in a healthy heart. In addition, MHV leads to increased levels of hemodynamic stress, thus undesirably stimulating thrombogenic conditions [30,31]. But MHV implantation can also result in platelet and red blood cell destruction.

Much work has been dedicated to the study of MHV hemodynamics, through direct experimentation and simulation, both in vitro and in vivo, for a wide range of MHV designs [32]. In addition, many investigators studied long-term clinical outcome in patients following aortic or mitral valve replacement by a mechanical prosthesis or bioprosthesis, as summarized by Rahimtoola [33,34]. These studies documented that, besides the hemodynamic and thrombogenic effects of the valve prostheses, comorbid conditions have key roles in clinical outcomes. However, these studies also revealed, but have not elucidated a considerable variance in the survival rates in cohorts of patients with different mitral valve replacements.

In this context, far less attention has been given to quantifying the effects of rotational orientation of MHVs in the mitral position and the resulting interactions between the filling jet and cardiac structure. Most importantly for the purpose of our study, it appears that a mitral MHV can impair LV diastolic filling efficiency if oriented arbitrarily [30,35]. Considering that tilting disc and bileaflet mitral MHVs generate highly directional flow patterns [36, 37] their implantation orientation has a direct effect on the resulting fluid-structure interactions. Given the directionality of MHV flow

dynamics, multiple imaging planes are necessary before the resulting hemodynamics can be accurately quantified, which so far has been one of the limiting factors for further investigations.

The primary focus of this work is on systematic in vitro tests utilizing a mechanical left heart model and a frequently clinically used bileaflet MHV (St. Jude Medical, Inc., St. Paul, Minnesota) placed in the mitral position. The goal was to quantitatively characterize LV fluid dynamics by vorticity and turbulent shear stresses at defined echocardiographic (echo) imaging projections for predetermined MHV angular positions, while maintaining constant heart rate and stroke volume.

4.2 Materials and Methodology

Testing was performed on a mechanical left heart model (ViVitro Labs, Inc., Victoria, Canada) (**Figure 4.1**). The model simulates the function of the left atrium, LV, and aortic root. Fluid such as saline or diluted glycerin (used to more closely approximate the viscosity of blood) circulates in a closed loop. The ellipsoidal LV is made of a homogeneous elastic polymer material that models the elasticity of the myocardium, allowing for expansion and contraction through the cardiac cycle. The left ventricle is completely submerged in a water filled chamber (called the hydraulic chamber) with a displacement pump fixed to one end of the hydraulic chamber. The pump displacement acts on the ventricle by causing it expand and contract with each pump cycle. Various waveforms can be used as inputs for the pump motion, including those that simulate a more natural cardiac rhythm. The left atrium compartment can be separated from the LV by a removable atrioventricular module, in which a tested mitral valve could be placed in

various angular positions. Similarly, the aortic root can be removed to allow placement of various aortic valves. In this study a tricuspid porcine valve was placed in the aortic valve position.

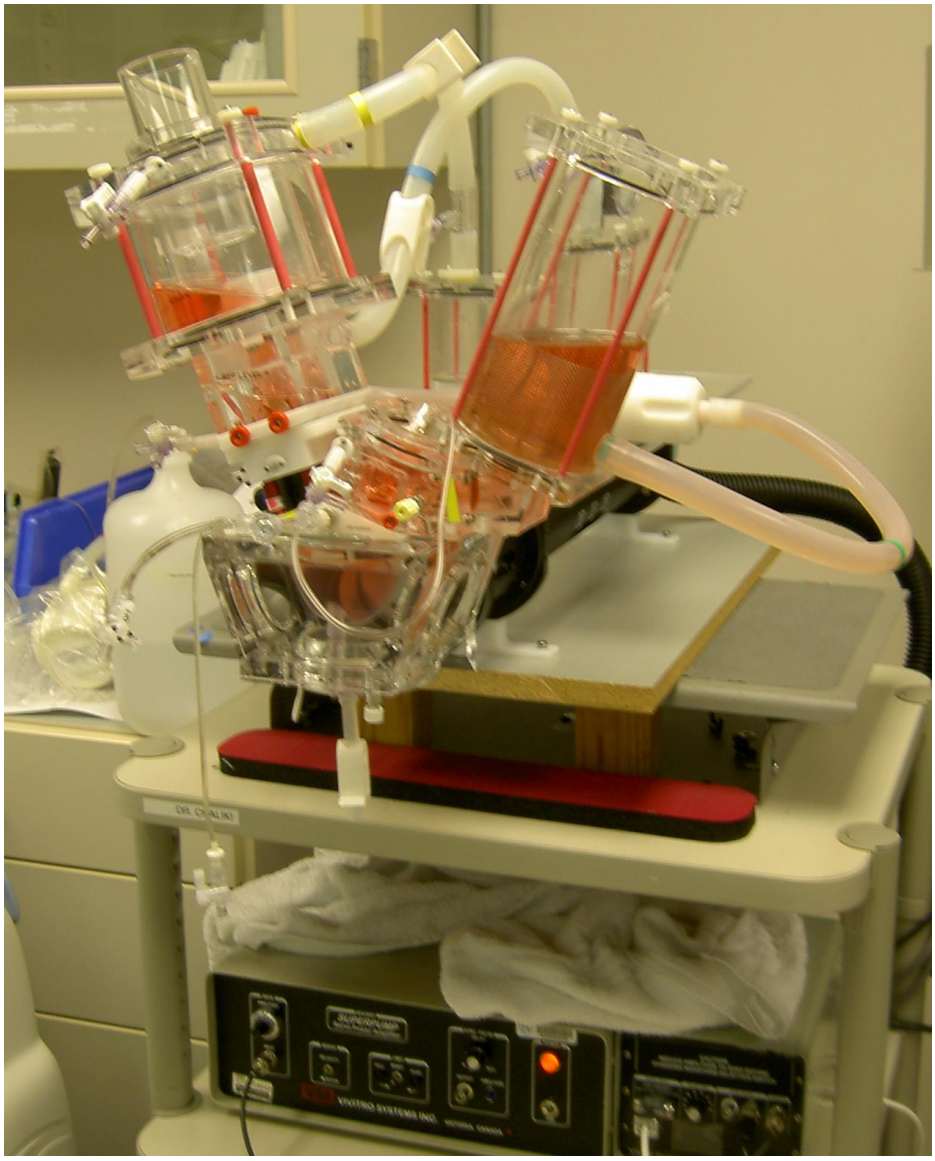

Figure 4.1. Photo of left heart model used in this study. On the upper right is the atrium, the lower center portion of the model is the LV and hydraulic chamber, the upper left is the aortic root. (ViVitro Labs, Inc., Victoria, Canada)

The ultrasound probe was positioned directly below the LV apex and data was acquired in four distinct imaging planes, each with 45 degrees of separation (**Figure 4.2A**).

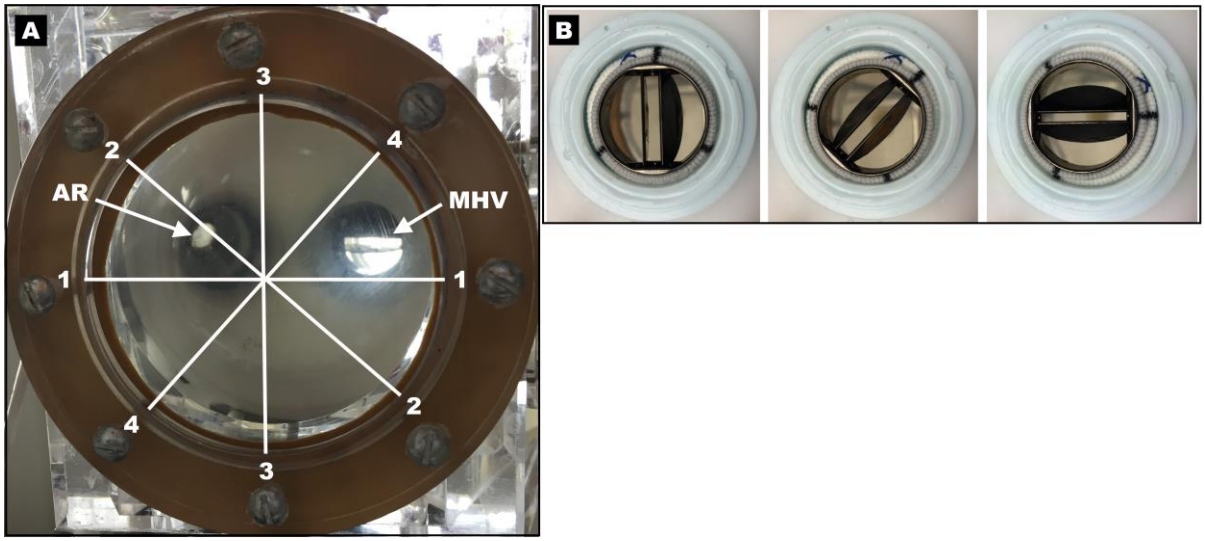

Figure 4.2. A) Photo of a partially disassembled mechanical left heart model showing a transparent elastic left ventricle (LV) viewed from the apex), the mechanical heart valve (MHV) and the aortic root (AR). Imaging planes are denoted by white lines and correspond to: 1 (90°), 2 (45°), 3 (0°), 4 (-45°). **B)** Placement of the bileaflet mechanical heart valve in the removable atrioventricular module in 0, 45, and 90 degree angular positions (viewed from the left atrium).

The selected valve was a St. Jude Medical bileaflet MHV with a 28 mm diameter which was placed in the mitral position. The studied angular positions of the mitral valve were 0, 45, and 90 degrees (**Figure 4.2B**) with respect to a plane intersecting the center of the aortic valve, LV apex, and the mitral valve. A pulsatile, sinusoidal flow was generated by an external pump that acted on the elastic LV from outside and produced two phases of controlled flow of saline through: 1) the aortic valve during “systolic” LV contraction (ejection phase) and 2) the mitral valve during “diastolic” LV expansion

(filling phase). Other LV phases that are present in a native heart, for example, isovolumic contraction and relaxation, or early and late filling, were not modeled. All data was collected during the transmitral filling period determined from the motion waveform of the external pump, which was set to simulate 70 beats per minute and a stroke volume of 70 ml.

Measurements were acquired using a cardiac ultrasound system Vivid 7 (GE Vingmed Ultrasound AS, Horten, Norway) equipped with a three-dimensionally (3D) scanning transducer (3V, GE Healthcare), which supported two-dimensional (2D) imaging with electronically rotated planes while the transducer itself was clamped in a fixed position. The rotational scans were projected through the existing ultrasound-transparent window in the mechanical model (**Figure 4.2A**). The window location allowed approximating clinical apical long-axis projections, ie, interrogating the heart from the LV apex towards the mitral and aortic valves. The scans were acquired in 1) a conventional (grayscale) B-mode to obtain "anatomical" projections through the LV and 2) a contrast-enhanced mode for imaging of Optison (GE Healthcare) microbubbles (**Figure 4.3A**) diluted 1:10 in saline. The ultrasound transmit power was set to 0 dB (ie, maximum "clinically-permissible" power) to obtain clear depiction of the microbubbles. It is noteworthy that in clinical settings, the transmit power (expressed as a mechanical index) is often reduced to minimize microbubble destruction during continuous scans because the overall dose that can be administered is limited. In our setting, however, the diluted microbubbles were added to the circulating saline solution in repeated boluses of 0.1 ml as needed. Continuous echo scans were collected through many heart cycles to

capture the microbubbles in optimal dilution and distribution to obtain high-quality scans for off-line microbubble tracking.

The tracking of the microbubbles ("particles") was done using PIVlab freeware [9](Thielicke) programmed in Matlab (The MathWorks, Natick, Massachusetts) and resulted in echo particle imaging velocimetry (PIV). Echo PIV [39, 40, 7] was used to generate and quantify velocity vector fields (**Figure 4.3B**) because of the ability to track particle motion without the need for visual access to the flow, which is typically necessary with optical PIV techniques that utilize a high-speed camera to visualize particle movement and a high-energy laser sheet to act as the flash. Echo PIV was performed off-line using the recorded echo DICOM images captured at 112 frames/s (ie, approximately 9 ms temporal resolution). Tracking through subsequent image frames included an adjustable multi-step pattern-matching search process resulting in generation of vector fields with an adequate range of detected velocities, such as in (**Figure 4.3B)**. PIV analysis was performed using a standard fast Fourier transform cross-correlation algorithm and Gaussian 2×3 point sub-pixel estimator. Interrogation window size is reduced iteratively from 64×64 to 16×16 pixels (3.54 pixels/mm) with a 50% overlap.

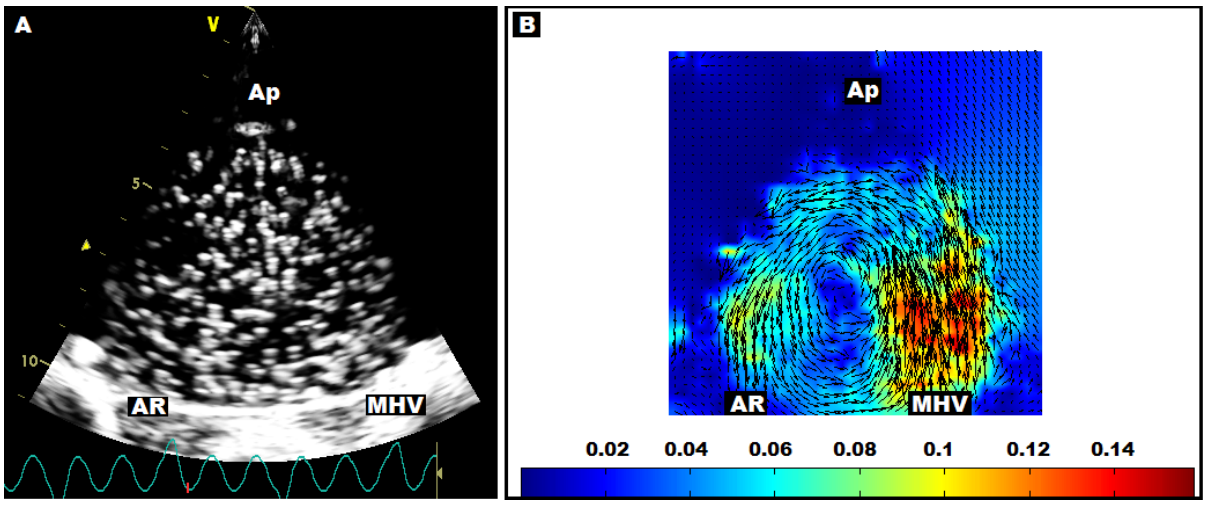

Figure 4.3. Representative scan (projection 3, valve angle 90 degrees) with **A)** Microbubbles, with mechanical heart valve (MHV), aortic root (AR), and LV apex (A) labeled. **B)** echo PIV velocity vector field (m/s) obtained by microbubble tracking averaged over series of images.

The velocity vector fields served for generation of shear and vorticity fields, again by using off-line processing in Matlab. We reconstructed the velocity, shear, and vorticity fields in four clockwise (as viewed from the LV apex) 2D projections electronically rotated in 45-degree increments:

Projection 1 (90 degrees; resembling a clinical "4-chamber" echo view);

Projection 2 (45 degree; resembling a clinical "2-chamber" echo view);

Projection 3 (0 degree; resembling a clinical "3-chamber" echo view); and

Projection 4 (-45 degree, ie, orientation perpendicular to Projection 2).

Using echo PIV, a 2D velocity vector field (such as the one demonstrated in (**Figure 4.3B**) was generated for each of the 4 echo projections and for each of the three mitral MHV angular positions. Therefore, we obtained twelve 2D velocity vector fields characterizing flow inside the LV during the period of transmitral "diastolic" LV filling.

Based on these velocity vector fields, we calculated the corresponding fluid vorticity and shear stress values.

Vorticity (ω) was calculated by taking the difference between the gradient of the y-component of velocity (v) with respect to the x-direction and the gradient of the x-component of velocity with respect to the y-direction:

$$\omega = \frac{\Delta v_y}{\Delta v_x} - \frac{\Delta v_x}{\Delta v_y}. \qquad (1)$$

Vorticity reflects the rotational hemodynamic movement inside the biological LV. Due to energy dissipation from viscous interactions, a well-defined single vortex (ie, a relatively high magnitude of vorticity) leads to less kinetic energetic losses than chaotic (turbulent) flow with many small vortices [41]. Previous studies have demonstrated that formation of the LV diastolic vortex could serve as an indicator of cardiac health [26].

Shear stress (τ) is directly related to the time-rate-of-strain (velocity gradient) of a fluid:

$$\tau_{xy} = \mu \left(\frac{\partial v}{\partial x} + \frac{\partial v}{\partial y} \right). \qquad (2)$$

Here, μ is the molecular viscosity coefficient of the fluid. Previous work [41]has established that high levels of shear stress will cause blood cell destruction or hemolysis in a biological heart [42].

The data was statistically analyzed for the LV filling period, during which the LV vortex is formed. PIV vector fields are temporally averaged over the LV filling cycle to minimize measurement noise. The numerical results of vorticity and shear stress are

expressed as means and standard deviation based on data from seven consecutive, temporally averaged filling cycles. One-way ANOVA was used for parametric comparisons of measurements obtained 1) at incremental angular mitral valve position for a given projection and 2) at incremental angular echo projections for a given angular position of the mitral valve. Paired comparisons between angular mitral valve positions at a given echo projection were assessed using paired two-tailed T-tests. Box-and-whisker plots , which show the median (center mark), the 25th and 75th percentiles (box edges) and the most extreme data not considered outliers (whiskers), were used for quick visualization of data distribution at given mitral valve angular position and echo projection and to reveal trends, if any, in the data as mitral valve or echo projection is incremented.

4.3 Results

The numerical results of vorticity and shear stress are summarized in (**Tables 1** and **2)**. In both tables, the negative values are a consequence of counterclockwise rotation of the flow in the original velocity vector fields.

In **Table 4.1**, the ANOVA p-values document a dependence of vorticity on both the echo projection and mitral valve position angles. Individual paired comparisons (marked by asterisks and crosses) indicate significant differences between mitral valve angular positions. However, a close observation of the individual measurements does not suggest any clear trend towards a systematic increase or decrease with mitral valve angular position.

Table 4.1. Results for Vorticity (1/s)

Projection #	Mitral Valve Angular Position			ANOVA P-value
	0 degrees	45 degrees	90 degrees	
1	1.906 (0.198)	0.646 (0.153)*	0.478 (0.174)*	<0.001
2	-1.631 (0.201)	-1.231 (0.133)*	-1.384 (0.186)*†	<0.001
3	-1.703 (0.144)	-2.058 (0.193) *	-2.593 (0.211)*†	<0.001
4	-3.678 (0.255)	-2.689 (0.196)*	-3.039 (0.223)*†	0.002
ANOVA, P-value	<0.001	<0.001	<0.001	

Results in parentheses represent standard deviation of the corresponding mean value.
*P<0.05 vs. 0 degrees
†P<0.05 vs. 45 degrees

Table 4.2. Results for Shear Stress (Pa)

Projection #	Mitral Valve Angular Position			ANOVA P-value
	0 degrees	45 degrees	90 degrees	
1	0.439 (0.12)	0.307 (0.102)*	0.254 (0.071)*	0.010
2	0.001 (0.114)	-0.031 (0.083)	0.317 (0.143)*†	<0.001
3	-0.431 (0.108)	-0.301 (0.101)*	-0.302 (0.091)*	0.040
4	-0.907 (0.105)	-0.485 (0.097)*	-0.679 (0.113)*†	<0.001
ANOVA, P-value	<0.001	<0.001	<0.001	

Results in parentheses represent standard deviation of the corresponding mean value.
*P<0.05 vs. 0 degrees
†P<0.05 vs. 45 degrees

In **Table 4.2**, a strong dependence of shear stress on both the echo projection angle and mitral valve angular position is again present (as in **Table 4.1** for vorticity) without a clear trend towards a systematic increase or decrease with mitral valve angular position.

The results in both **Tables 4.1** and 4.**2** demonstrate that angular orientation of the mitral valve is a critical factor in producing flow shear and vorticity, without any clear

trend with regard to an incremental change in the valve angular orientation. Furthermore, the ANOVA of values of vorticity and shear stress for any given mitral valve angular position clearly shows that the magnitudes of the two tested parameters are strongly influenced by the used projection.

Distribution of shear and vorticity values, as visually represented by box-and-whisker plots in **Figures 4.4A** and 4.**4B**, respectively, confirm that both the mitral valve angular position and the used echo projections affect the results, and that there is no clear systematic trend in the values with respect to angular placement of the mitral valve.

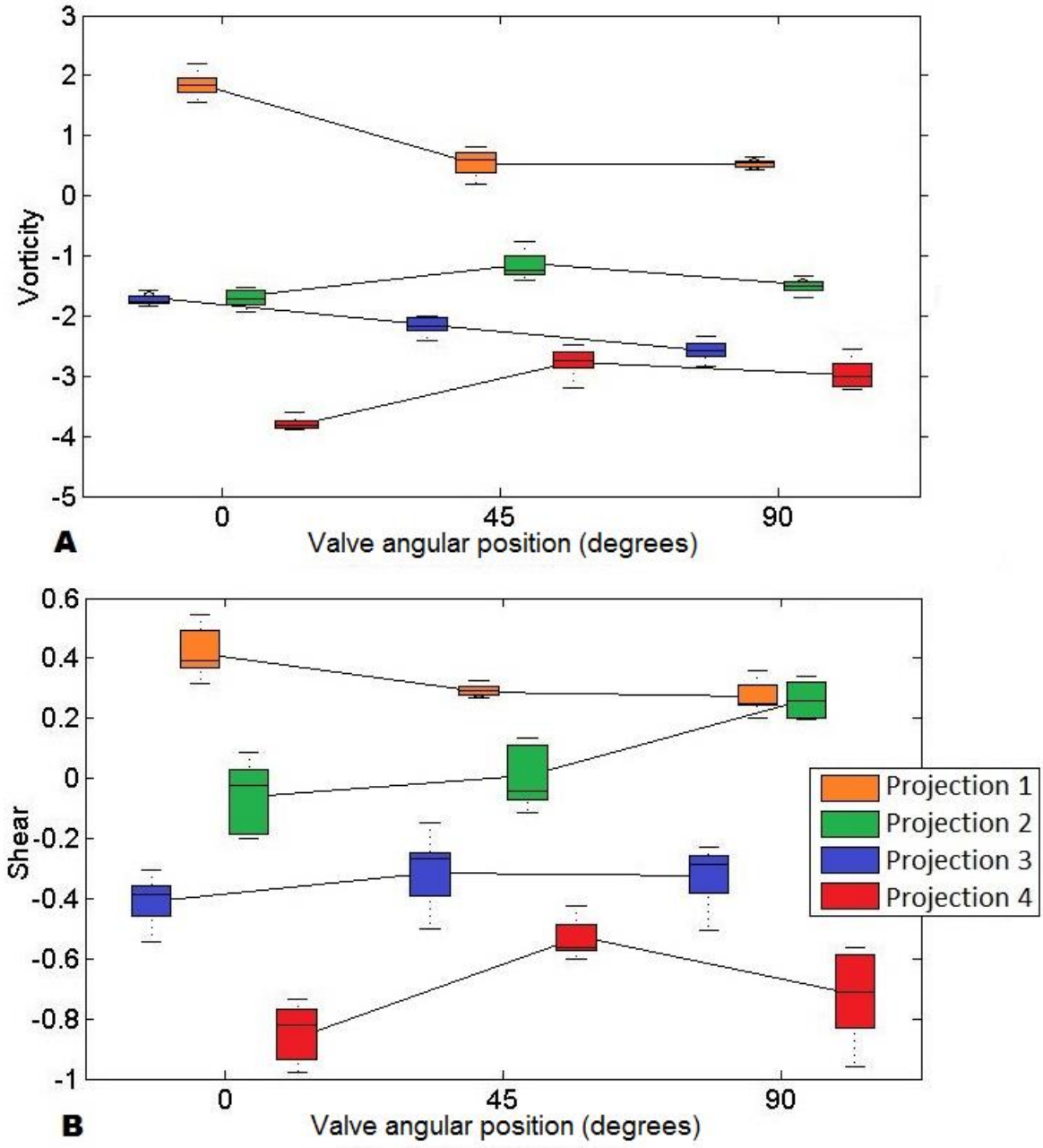

Figure 4.4. Box-and-whisker plots. Change in **A)** vorticity (1/s) and **B)** shear stress (Pa) with respect to the mitral valve angular position at each tested echo projection.

Based on mean values in **Tables 4.1** and 4.**2**, images in **Figure 4.5** are illustrative examples of 2D intraventricular flow vorticity and shear stress fields with the lowest and

highest magnitudes. While a high vorticity and low shear stress magnitudes of intraventricular flow would be beneficial, the results obtained in our model did not reveal any clearly "optimal" mitral valve angular position that would combine the two desirable conditions.

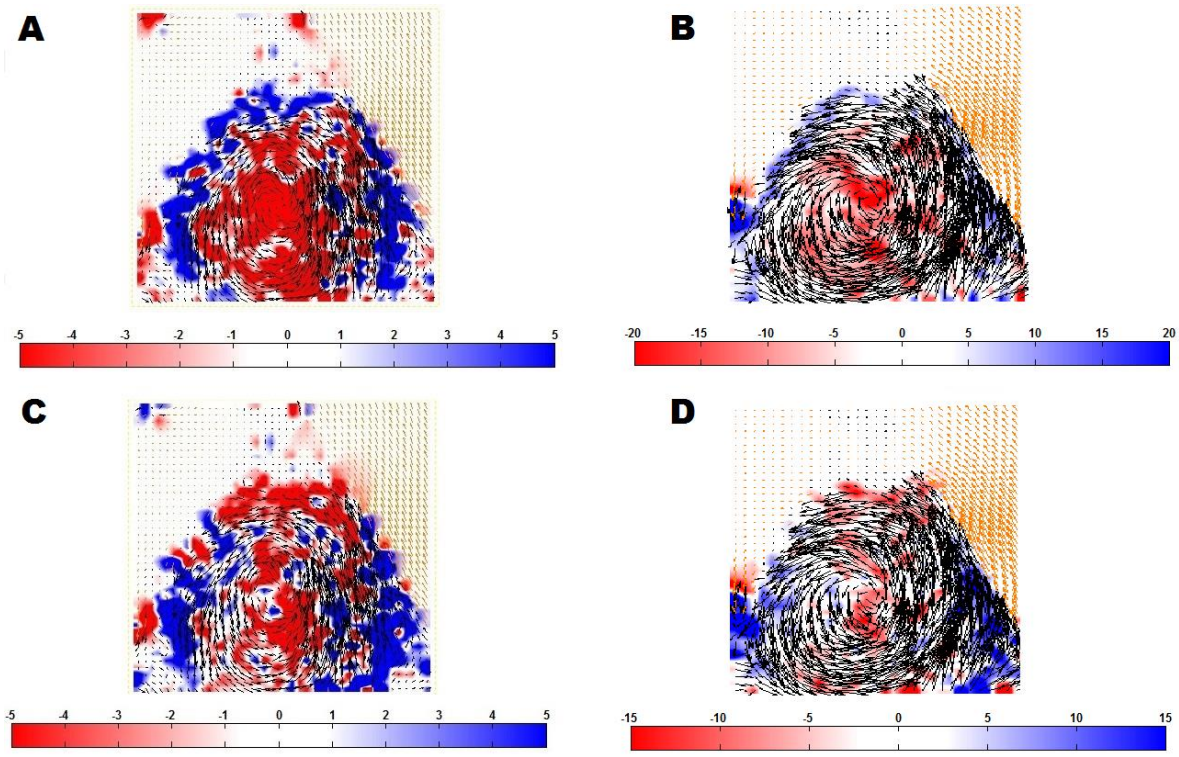

Figure 4.5. Vector flow fields temporally averaged over inflow period with A) lowest vorticity magnitude (1/s; projection 1, valve at 90 degrees), B) highest vorticity magnitude (1/s; projection 4, valve at 0 degrees), C) lowest shear stress magnitude (Pa; projection 2, valve at 0 degrees) and D) highest shear stress magnitude (Pa; projection 4, valve at 0 degrees).

4.4 Discussion

The main finding of this experimental study, which utilized an elastic mechanical model of a beating LV and a bileaflet MHV in the mitral position, is that the rotational

position of the valve is a critical determinant of the LV flow characteristics. This finding is important in the context of other studies that implied the importance of the prosthetic valve rotational orientation on the downstream turbulence and risk of microembolization using both in vivo experimentation and computational methods [43, 44] as well as animal studies [45]. So far, however, existing research has focused on anatomical and anti-anatomical rotational orientation of MHVs using fixed two-dimensional (2D) ultrasound and MRI imaging planes [31, 44, 45]. Our study extends these results by showing the significant effect of 45-degree incremental rotational positioning of the mitral valve on intraventricular flow patterns, vorticity, and shear stresses.

Furthermore, it is demonstrated that selection of a 2D projection for visualization of velocity vector patterns or quantitation of vorticity and shear stresses, which are indeed complicated 3D intraventricular flow phenomena, is another critical factor. In several studies investigating LV hemodynamics influenced by MHV orientation, only a single imaging plane has been utilized and calculations were based on optical-PIV, echo-PIV, or MRI data obtained within that plane [43,31]. This study implies that to fully quantify mitral MHV performance based on rotational orientation, it is necessary to obtain data from all standard echo imaging planes. Clearly, using just one projection could be significantly misleading in assessing hemodynamic impact, such as the magnitude of vorticity and shear stress. It is speculated that it may be necessary to not only use the standard projections but, in fact, come up with additional "non-standard" projections optimized for evaluation of hemodynamic patterns and parameters.

Noticeably, projections 2 and 4 (ie, perpendicular projections at 45 and -45 degrees, respectively) did not produce opposite shear and vorticity values with the same

magnitude. It is possilbe that there was some asymmetricity in the LV shape, transvalvular flow, off-axis aiming of the ultrasound transducer, or combination thereof, which would be the case also in a clinical setting. Ideally, the evaluation should be performed in a fully 3D echo imaging mode. Although the current real-time 3D ultrasound imaging systems have recently made tremendous technological advances, they still do not provide sufficient temporal resolution for analyses of transmitral and intraventricular fluid dynamics.

The results do not clearly convey an "optimal" bileaflet mitral MHV angular position, which would be characterized by a well-developed diastolic rotating fluid mass (ie, high magnitude of vorticity) with low shear stresses. Although, close assessment of the magnitudes in (**Tables 4.1** and 4.**2)** and, especially, visual inspection of some trends in (**Figure 4.4)** suggest that an angular position of the mitral valve between 0 and 45 degrees approaches to some extent the desirable combination of high vorticity with low shear stresses. In this context, it is of note that the two tested parameters, ie, vorticity and shear stress, although they have a different physical meaning, have been derived from the same source data (ie, velocity vector fields) and thus, may not be entirely independent. Simulation of cardiac performance at various heart rates, stroke volumes, and pressure loading would have likely shed more light on the mitral angular position for optimal fluid dynamic performance.

The limitations of this study are that the measurements were influenced by the lack of the right ventricular cavities and pulmonary circulation, and the simplified "anatomy" of the elastic LV lacking, for example, native cardiac wall, papillary muscles, trabecules, or considerable natural asymmetric shapes of the LV and its outflow tract.

Implantation of the MHV into a native (porcine or dog) beating hearts ex vivo or in vivo at different angular positions of the mitral would alleviate the aforementioned limitations, although at a cost of reduced or no control to achieve perfectly constant hemodynamic conditions during measurements, as we could during the current study. Another limitation is that the results were not obtained during systematically changed loading conditions. In our present model, these interventions were not entirely separable and, therefore, we elected to conduct this initial study under a well-defined single steady-state condition.

Clinically, replacement of a severely damaged and hemodynamically detrimental native mitral valve by a mechanical prosthesis is an important therapeutic solution. However, suboptimal "arbitrary" angular positioning of the mitral prosthesis may have an undesired effect on intraventricular hemodynamics. For instance, impared generation of the intraventricular vortex ring is now recognized as a contributing mechanism of diastolic dysfunction in patients with hypertrophic cardiomyopathy [46]. Consequently, impairment of the natural diastolic vortex flow by the suboptimal positioning of the MHV could result in kinetic energetic losses or have thrombogenic effects, and may therefore undesirably affect the long-term clinical outcome.

4.5 Conclusion

This initial study strongly suggests that angular positioning of the mechanical mitral valve is an important determinant of intracardiac hemodynamic conditions. Furthermore, it is demonstrated that a comprehensive understanding of LV dynamics is necessary to fully quantify mitral valve performance. The LV flow is a complex and strongly three-dimensional. When studying the left intraventricular flow using two

dimensional imaging techniques that fail to resolve the three dimensionality of the flow, it is possible that incorrect assumptions can be made. This study demonstrates that using a single two dimensional plane to quantify MHV performance is unacceptable and can lead to incorrect conclusions about the preferred positioning of an MHV.

With the advent of improved ultrasound system, particularly those that allow for three dimensional imaging with high spatial and temporal resolution, it will likely be possible to fully quantify the LV flow. Additionally, a better understanding of the interactions between blood flow and heart walls is also necessary to quantify MHV performance. Studies need to be done ultimately leading to optimization of mitral valve angular placement, and, thus, contributing to long-term patient life quality and survival.

Chapter 5

ELASTICITY ESTIMATION USING OPTICAL PARTICLE IMAGE VELOCIMETRY VELOCITY FIELDS

This chapter focuses on the development of a novel technique for estimating the elasticity of a thin, cellulose acetate flap using forcing data derived from optical PIV velocity fields. A flap is affixed to a stand, submerged within a water-filled tank, and deformed using a water jet pulse. PIV is then performed at the interface between the thin film and water jet throughout the deformation cycle; the resulting velocity field allows the determination of localized forcing measurements along the film surface. An optimal estimation technique is coupled with a finite element analysis (FEA) program to determine the flap's elasticity. Results show good agreement with actual elasticity measurements for both homogeneous and non-homogeneous elasticity thin-film sheets. In addition, a quantitative study is performed to determine the optimal vector density for a given element size to achieve an accurate elasticity estimation value.

5.1 Introduction

The ability to accurately measure the cardiac structure noninvasively is critical for the development of early diagnostic techniques [47]. Determining localized changes in elasticity of the mitral valve, for instance, would aid in clinical diagnosis of mitral valve prolapse or additional valve pathophysiology [48]. Various methods have employed *in vivo* measurements for determining cardiac elasticity [49]; however, these techniques are for experimental purposes only and not for use as a diagnostic technique.

Several techniques have been developed that allow for *in vitro* measurements of blood flow dynamics. In particular, echocardiographic particle imaging velocimetry (echo-PIV) [13, 25, 29, 50] stands out as cost-effective with high temporal resolution and ease of use. Described by Shandas's group [25,8], echo-PIV is well suited for tracking the complex spatial features of intracavitary blood flow using contrast microbubbles captured in sequences of high-frame-rate two-dimensional (2D) brightness-mode ultrasonographic images [47, 9]. In essence, echo-PIV is a result of processing with software designed for optical-PIV analysis that can also track the brightness signals generated by the microbubbles in the serial image frames. To obtain local flow velocity vectors and velocity maps, the software calculates displacements of microbubbles over a given time interval, which is typically determined by the actual frame rate.

As a step towards practical applications of optical- and echo-PIV methods, this paper presents a methodology for estimation of elastic properties of materials immersed in a flow, by using velocity field measurements only. Such an approach can be invaluable

to noninvasive estimations of elastic properties of cardiac valves or tissues *in vivo*. To validate our approach, we use a cellulose acetate film immersed in water and deform the film by a jet pulse. The Young's modulus of a particular material is estimated using forcing data generated from optical-PIV velocity fields. Considering the fundamental similarity between optical- and echo-PIV, the success of elasticity estimation using optical-PIV implies that elasticity estimation with echo-PIV should also be possible, provided accurate velocity fields can be generated. In addition, considering the elasticity of the mitral valve, particularly a diseased valve, is non-homogeneous [51, 52], the elasticity estimation of non-homogeneous thin sheets employed in this study closely simulates clinical conditions of a leaflet exposed to blood flow.

The process of estimating the elasticity is carried out in three distinct routines: data acquisition using an optical-PIV method, forcing determination using flow velocity data, and the use of an estimator coupled with a Finite Elements Analysis (FEA) program to determine the elasticity. The process is detailed in Figure 1 and a more thorough description is provided in the next section.

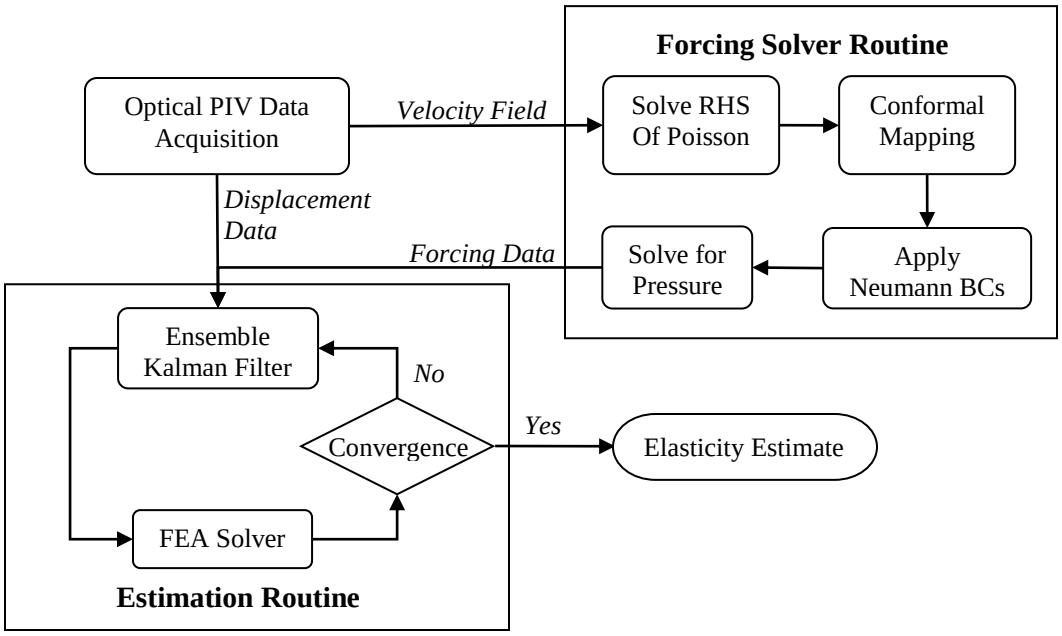

Figure 5.1 Flow chart indicating the steps required for elasticity estimation using velocity field and displacement data acquired from PIV

5.2 Materials and Methods

This section outlines the development and implementation of each section of the elasticity estimation routine detailed in **Figure 5.1**. Velocity data obtained from PIV is input to a forcing solver routine. This allows the determinations of a pressure field from the velocity field, and thus the determination of forcing. The forcing and displacement data, which is obtained based on visual inspection, is input into the elasticity estimation routine. The estimation routine determines the optimal elasticity based on repeated sampling of a finite element analysis model with the known forcing and displacement, and varying elasticity "guesses".

5.2.1 Optical Particle Image Velocimetry

PIV is a velocity field measurement technique that calculates the velocity of neutrally buoyant tracer particles seeded within the flow. An optical-PIV system consists of a high-speed charge-coupled device (CCD) camera that is synchronized with a 700mJ, argon-ion laser that acts as the 'flash' when imaging. The laser light reflected by tracer particles provides contrast from background noise and the particle movement is then tracked between image sequences. The optical-PIV measurements in this study are obtained using a LaVision acquisition system and DaVis software (LaVision GmbH, Göttingen, Germany).

The velocity is measured by tracking particle displacement between a set of two, high-speed images recorded by the camera, where the time step between images is dependent upon flow velocity and window size. The optical-PIV system pauses for an increased time step until taking an additional image pair. The determination of particle displacement between image pairs, for a given time step, leads to the calculation of flow velocity. The PIV setup used for this particular experiment utilizes a single camera to capture data; allowing the determination of two-dimensional data.

The images are processed using DaVis software, version 7.2.2.80. A Fast Fourier Transform (FFT) cross-correlation technique is applied and images are processed using an iterative scheme with multiple passes of decreasing interrogation window size. For

each iteration, the corresponding window size and weight, percent overlap, and number of passes can be selected.

5.2.2 Experimental Apparatus

A flexible plastic film (7mm wide, 2cm long, .1mm thick, E = 0.45GPa) is attached to a stand and submerged in water filled tank (**Figure 5.3**). The flap is then deformed with 200ms pulse of water generated using a 20W aquarium pump rated at 30 GPM at 0 head. The exit orifice diameter and width of the flap were chosen so that (1) laminar flow would traverse over rather than around the flap, thereby making the flow primarily two-dimensional, and (2) the laser sheet (approximately 6mm thick where it contacts the deformed, steady-state film surface) encompasses the flow entirely.

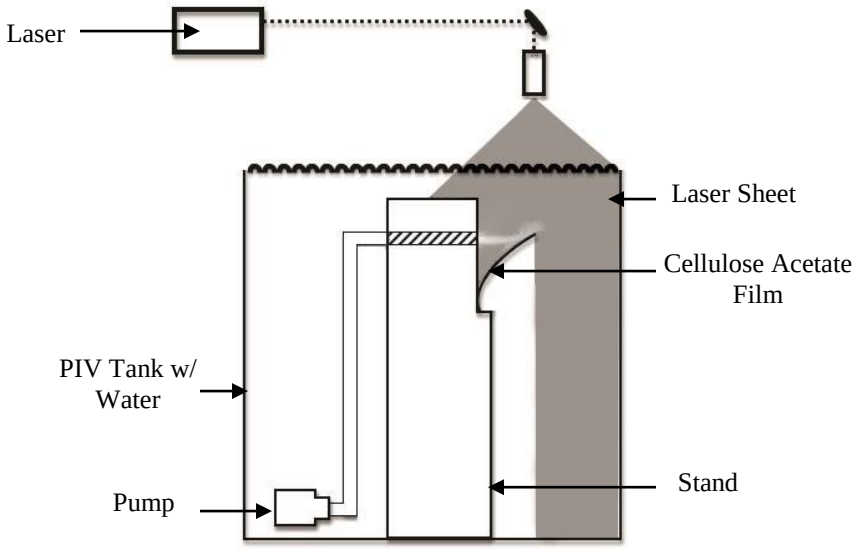

Figure 5.2 Setup employed to determine forcing values using PIV measurements

The laser sheet (as indicated in gray in **Figure 5.3**) is projected downward from above the tank and spread using a concave lens.

Images are captured for the opening and closing process and velocity fields are generated from the images using PIV software. A 200 ms jet duration was chosen so that, after the film is fully deformed (approximately 100 ms after the jet start), a 'steady state' is achieved where laminar flow over the film surface remains relatively constant with respect to time and the film remains in the deformed position for 100 ms. The Reynolds number, based on film length, for the steady state condition is approximately 10,000. The velocity vectors obtained over this 100 ms duration are then temporally averaged to minimize out-of-plane movement; thereby allowing for a static rather than transient FEA analysis

Using a 1,376 x 1,040 pixel ImagerIntense CCD camera, the field of view was 52 x 41mm^2. Given the pulse separation of 174 μs and a maximum jet velocity of 1.05 m/s, the maximum particle displacement is 4.8 pixels. The images were processed by the DaVis software using the iterative cross-correlation technique with decreasing interrogation window size. The maximum window size was 256 × 256 pixels with 50% overlap and 2 passes, and the minimum window size was 32 × 32 pixels with 75% overlap and 2 passes. Approximately 8 particle pairs were evident per interrogation window. Weighting factors were not applied to either window size. Vectors with magnitude exceeding two times the root-mean-square magnitude of neighboring vectors were automatically labeled as outliers and deleted. An example of the resulting

instantaneous velocity field is shown in **Figure 5.3**. It is evident that the flow remains primarily laminar over the surface of the film, the transition to turbulence begins at the tip.

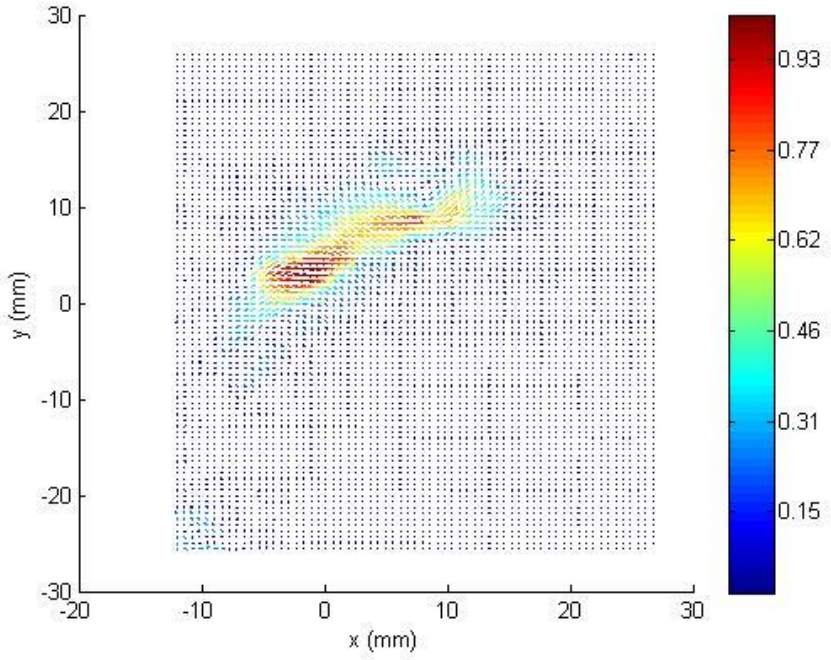

Figure 5.3 Instantaneous PIV velocity field for flow over thin film surface. Velocity in m/s and spatial resolution in mm

5.2.3 Computation of Forcing Based on Velocity Vector Fields

Using the Navier-Stokes equations for incompressible flow, determination of the pressure field is possible based on PIV velocity field measurements [53]. Recent work by Charonko et al [54] quantitatively assessed the three primary approaches used to derive pressure fields from velocimetry data. These techniques are: (1) integration of pressure

gradients as derived using the Navier Stokes equations, (2) solution of the pressure Poisson equation boundary value problem, and (3) CFD modeling based on PIV data.

Starting with the Navier-Stokes equations for incompressible flow,

$$\nabla P = -\rho\left(\frac{\partial u}{\partial t} + u \cdot \nabla u\right) + \mu\left(\nabla^2 u\right) + F \tag{5.1}$$

Where *p* is pressure, *u* is the velocity vector, μ is a constant viscosity, ρ is constant density, and *F* is a vector field representing body forces such as gravity or centrifugal force. The pressure gradient can readily be calculated using 2D PIV velocity data to solve for terms on the right hand side. Through the application of numerical integration techniques to the pressure gradient field, the pressure field can then be determined over the entire flow domain. This requires starting from a direct pressure measurement, or expected pressure measurement, and then integrating over single or multiple paths. Typically, averaging is performed between multiple paths or between multiple pressure fields solved with varying initial conditions; this process tends to smooth errors accumulated in the solution process due to inconsistencies in the velocity data [54].

For all solution techniques, errors in the PIV velocity data pose a significant problem. Charonko et al. demonstrated that, even for relatively small errors, the derived pressure fields quickly became unusable [54]. In applications with steady state flow, where studying flow dynamics in a mean rather than instantaneous nature is acceptable,

the data can be time averaged to minimize measurement noise. Taking the time average of Eq. 1 and writing in tensor notation, results in: [55]

$$\frac{\partial \overline{p}}{\partial x_i} = -\rho \overline{u}_j \frac{\partial \overline{u_i}}{\partial x_j} - \rho \frac{\partial \overline{u_i' u_j'}}{\partial x_j} + \mu \frac{\partial^2 \overline{u_i}}{\partial x_j \partial x_j} \tag{5.2}$$

Where the overbar indicates time averaged properties. The right hand side is comprised of mean momentum, turbulent momentum (fluctuating components), and viscous stress terms. These can be computed using averaged and statistical data derived from 2D PIV measurements and the time averaged pressure field can be determined using an aforementioned integration scheme.

From the instantaneous velocity fields generated by optical-PIV, it is also possible to determine pressure through the application of the pressure Poisson equation. The Poisson equation is found by taking the divergence of Eq 1. and by applying the incompressibility form of the continuity equation, given by:

$$\nabla \cdot u = 0 \tag{5.3}$$

The result is the pressure Poisson equation,

$$\nabla^2 P = -\rho \nabla \cdot \left(u \cdot \nabla u \right) \tag{5.4}$$

This can be solved as a boundary value problem with either Neumann or Dirichlet boundary conditions.

Previous work [53,54] has demonstrated that the solution of the Poisson equation is highly susceptible to errors due to out of plane particle movement and other data anomalies. This is primarily due to the application of the continuity equation to the divergence of the Navier-Stokes equations, which creates third order derivatives that amplify error in the measured data.

Second-order central difference approximations were used to discritize the PDE's, the Poisson equation can then be solved on a non-staggered, regular grid. The accuracy of this technique is detailed by Gurka et al [53] and Charonko et al [54]. Neumann boundary conditions were applied to the film/water interface along with the other boundaries. Schwarz-Christoffel mapping is applied to transform the irregular geometry Fig 4. (a) into a rectangular grid via conformal mapping Fig 4. (b) on which the two dimensional Poisson equation can be solved. This grid offers high spatial resolution along the flap surface. The Schwarz-Christoffel toolbox (version 2.3) developed by Tobin Driscoll and used to generate the conformal transformations [55]. To avoid excessive interpolation errors, the grid size should correspond to the resolution of the velocity field. In this case, pressure was solved on a 40x40 grid.

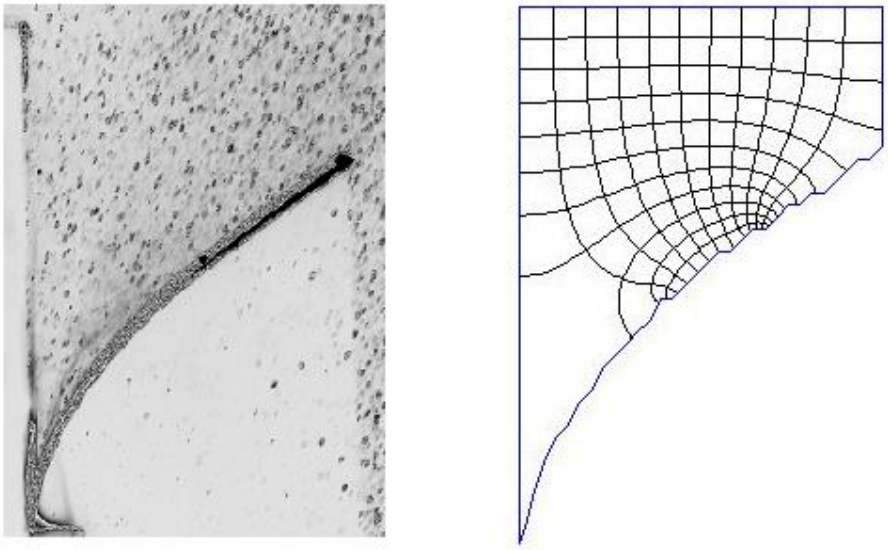

(a) (b)

Figure 5.4 Physical location of fully deformed flap (a); mapped canonical domain for deformed flap (b), note: mesh density is reduced in this image

The film is then divided into segments and the forcing distribution along its length can be determined from the local pressure measurements through $F = pA$, where p is the average value of the pressure along each segment of the film (a total of 40 segments were used) and A is equivalent to the surface area of each segment exposed to the corresponding pressure. Considering the width of the jet was selected to match the film width, the entire area of each segment was assumed to be exposed to the corresponding pressure.

5.2.4 Finite Element Analysis

Euler-Bernoulli (classical) beam theory with Hermitian elements is employed to determine the elasticity of both the homogeneous and non-homogeneous films. Considering only two-dimensional data is available from the optical images, three-

dimensional models would be underdetermined and predictions about the geometry would be required. The use of quadrilateral or linear triangular plane stress elements would be possible; however, because of the high aspect ratio of the thin film geometry (the length is considerably greater than the thickness), a prohibitively high number of elements would be required to preserve the element aspect ratio (generally around 1).

Euler-Bernoulli beam theory was selected for this FEA analysis because of the fast computational time and relatively accurate analysis. Unlike Timoshenko beam theory, Euler-Bernoulli beam theory does not account for the effects of transverse shear strain; however, considering the high aspect ratio of the geometry, these effects are of minor importance [56]. Hermitian beam elements are used with two degrees of freedom per node: transverse deflection and slope. A brief derivation of the FEA equations for Hermitian beam elements is provided [57]. The bending equation for Euler- Bernoulli beam theory is

$$\rho \frac{\partial^2 v}{\partial t^2} + \frac{\partial^2}{\partial x^2}\left(EI \frac{\partial^2 v}{\partial x^2} \right) = q(x,t) \tag{5.5}$$

Where E is the Young's modulus, I is the inertia, v(x,t) is the transverse displacement and q(x,t) is a pressure loading along the beam that is both spatially and time dependent. The Galerkin method of weighted residuals is applied to the beam equation to derive the element equations for the finite element analysis. The averaged weighted residual of the bending equation is given by

$$I = \int_0^L \left(\rho \frac{\partial^2 v}{\partial t^2} + \frac{\partial^2}{\partial x^2}\left(EI \frac{\partial^2 v}{\partial x^2} \right) - q(x,t) \right) w dx = 0 \tag{5.6}$$

Where L is the beam length and w is a test function. Discretization of the beam into Ω elements gives

$$I = \sum_{i=1}^{n} \left(\int_\Omega \rho \frac{\partial^2 v}{\partial t^2} w dx + \int_\Omega EI \frac{\partial^2 v}{\partial x^2} \frac{\partial^2 w}{\partial x^2} dx - \int_\Omega q w dx \right) + \left[Vw - M \frac{\partial^2 w}{\partial x^2} \right]_0^L = 0 \tag{5.7}$$

Where V is the shear force and M is the bending moment. Each element has two end nodes, where each node has variables for transverse deflection v and slope θ; this gives a total of four degrees of freedom per element. Two connecting elements must have continuous deflection and slope at the common nodal point. Continuity along elements can be accomplished using Hermitian cubic shape functions. The interpolation formula for the transverse deflection of a beam element with length l is given by

$$v(x) = H_1(x)v_1 + H_2(x)\theta_1 + H_3(x)v_2 + H_4(x)\theta_{21} \tag{5.8}$$

Where

$$H_1(x) = 1 - \frac{3x^2}{l^2} + \frac{2x^3}{l^3}$$

$$H_2(x) = x - \frac{2x^2}{l} + \frac{x^3}{l^2}$$

$$H_3(x) = \frac{3x^2}{l^2} + \frac{2x^3}{l^3}$$

$$H_4(x) = -\frac{2x^2}{l} + \frac{x^3}{l^2}$$

The stiffness matrix for the beam element is found through the application of Galerkin's method and Hermitian shape functions to $\int_\Omega EI \frac{\partial^2 v}{\partial x^2} \frac{\partial^2 w}{\partial x^2} dx$.

$$K = \int_0^l B^T EIB dx \tag{5.9}$$

Where

$$B = [H_1^{''} \quad H_2^{''} \quad H_3^{''} \quad H_4^{''}]$$

Eq. (6) can be modified for an instance where the elasticity is non homogeneous along the beam length. An equation for a distributed pressure forcing can be derived from $\int_\Omega qwdx$. The forcing matrix is found from

$$F = \int_0^l q(x) B^T \tag{5.10}$$

Finally, the nodal displacements *d* for the finite element system can be solved from the stiffness and forcing matrices using the following relation

$$Kd = F \tag{5.11}$$

5.2.5 Parameter Estimation: The Ensemble Kalman Filter

An Ensemble Kalman Filter [58] is used to estimate elasticity. The standard structure for the model to be estimated is

$$d_{k+1} = f\left(F, E_k\right) + w_k \tag{5.12}$$

$$E_{k+1} = E_k + w_k' \tag{5.13}$$

$$y_k = d_k + v_k \tag{5.14}$$

Where *k* counts the iteration of the model, d_k is a state vector containing the plate displacements, E_k is the current estimate for the elasticity; the first equation in the standard form represents the solution of eq. (11) using the forcing F calculated from PIV data; the second equation is added to the standard model and it expresses the fact that the elasticity E_k being estimated is a constant; the last equation is conventionally called the measurement equation, in estimation theory. The noise terms w_k, w_k' and v_k are generated

white Gaussian noise that is associated with modeling and measurement errors. Their covariance matrices, *Q, Q'*, and *R* respectively, govern the performance of the estimator.

An Ensemble Kalman filter is structurally similar to a linear Kalman filter [59], with an important difference: the linear Kalman filter evolves a *covariance matrix* for the estimations together with the estimations themselves, and the modeling and measurement noise are assumed to be Gaussian; the ensemble Kalman filter evolves an *ensemble* of potential candidate solutions, rather than providing an explicit equation for evolving the covariance matrix for the estimations. This eliminates the necessity to operate on a linear, or linearized, model. Full details on the implementation of the Ensemble Kalman Filter are given in [58]. The primary focus is on the choice for the matrices *Q, Q'* and *R*, that is crucial to ensure that the estimator works correctly. For all cases, 100 ensemble points are used, and it was found that this number had negligible effects on the accuracy of the estimations.

Since the measured displacements are used to calculate the estimation error, the natural choice for the measurement covariance matrix *R* is to define it as a diagonal matrix of the variances of the actual deformation measurements; those variances are estimated by analyzing 8 snapshots of the plate, taken when it was close to its maximum extension.

The covariance of the state model is determined from the ensemble set. For the homogeneous flap using three elasticity estimates, the covariance *Q'* of the elasticity and the initial guess $\hat{x}$ were chosen as:

$Q' = diag[1 \quad 1 \quad 1] \text{x} 10^{7}$ and $\hat{x} = [1 \quad 1 \quad 1] \text{x} 10^{8}$

For the non homogeneous flap, the values are:

$Q' = diag[20 \quad 10 \quad 1] \text{x} 10^{7}$ and $\hat{x} = [10 \quad 10 \quad 1] \text{ x} 10^{8}$

It was necessary to increase the initial guess for the stiff portion of the non homogeneous flap to ensure stability in the estimator routine. Considering the difference between the elasticities of the more and less stiff regions on the film is an order of magnitude, it is possible to theorize that the initial guess must always be within an order of magnitude from the true elasticity.

5.3 Results

Three separate tests were conducted to determine the overall effectiveness of the elasticity estimation technique. The first test is performed using a thin film with a homogeneous elasticity of $4.5 \text{x} 10^{8}$ Pa. The elasticity estimation process is designed so that one elasticity value will be applied to the 30 beam elements. The second test also uses a thin film of homogeneous elasticity; however, for this case, the elasticity estimation code is altered so that three separate elasticity values are computed along the beam length. The first third of the beam will share one particular elasticity (E1) the next third of the beam will share an elasticity (E2) and the final third of the beam will share an elasticity (E3). The estimator will then determine which combination of E1, E2 and E3 matches the actual deformation. When testing the film with uniform elasticity, the values

of E1, E2, E3 should be equivalent. The final test involves a film with non-homogeneous elasticity, half of the film has elasticity 4.5×10^8 Pa and the other half has elasticity 3.6×10^9 Pa. The model will be discretized using three elasticities E1, E2 and E3. This will test the ability of the elasticity estimator to detect changes in elasticity along the length of the film.

The outputs of the ensemble Kalman filter for the three tests are shown in the following figures and the results are summarized in Table 5.1. In each case, a certain initial value for the elasticity is chosen that is sufficiently far from the actual value yet still allows for convergence after 100 iterations.

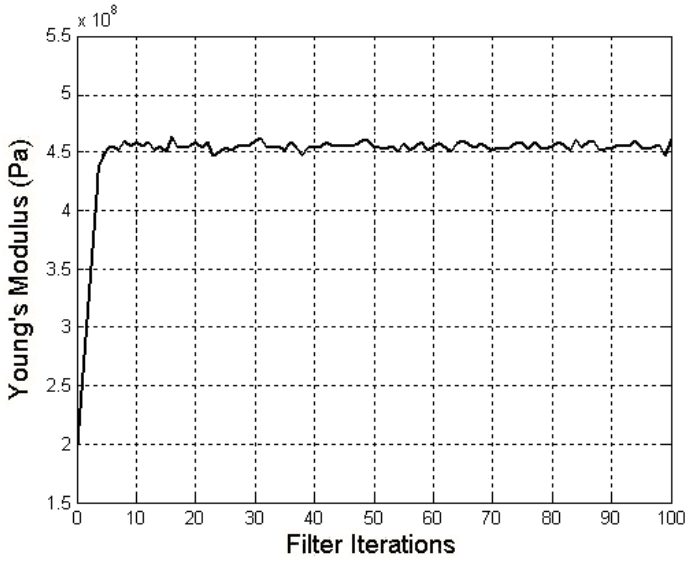

Figure 5.5. Elasticity estimation for a film of homogeneous elasticity using a single elasticity model. The filter estimate is within 2% of the true solution of 4.5×10^8 Pa. The standard deviation for the estimate is +/- 2.5×10^7 Pa.

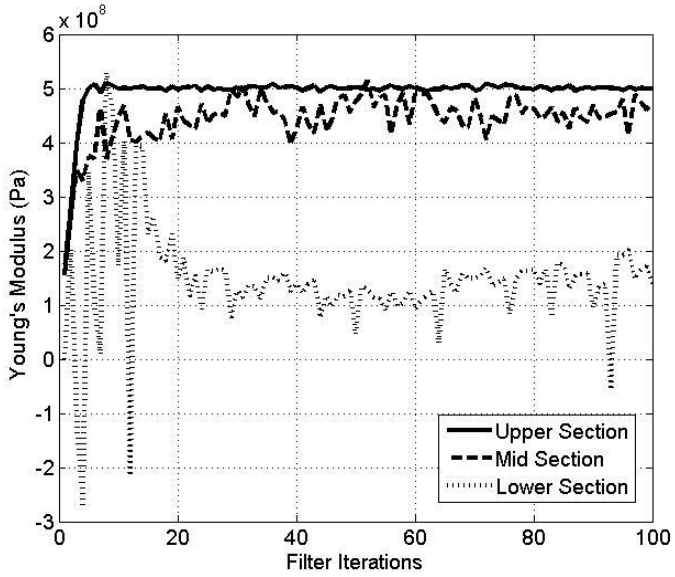

Figure 5.6 Elasticity estimation for a film of homogeneous elasticity using three separate elasticities in the FEA model. The estimated elasticity of the upper section and mid section are within one standard deviation of the actual elasticity value of 4.5×10^8 Pa. The estimated elasticity of the lower section is within two standard deviations of the actual value.

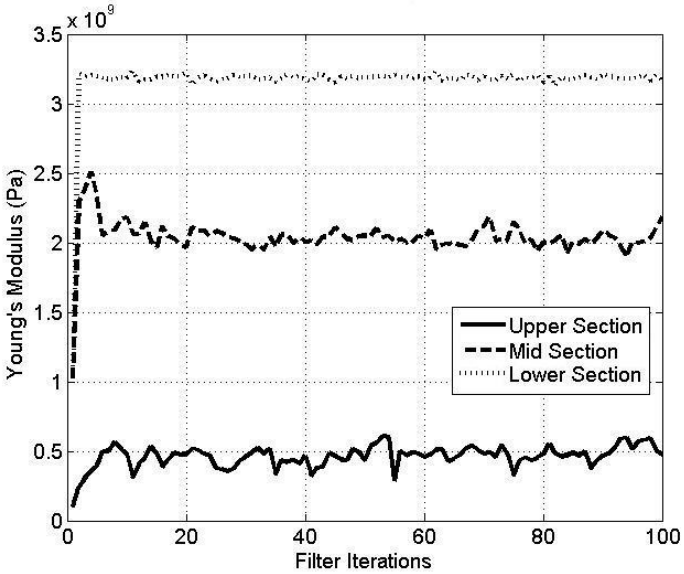

Figure 5.7 Elasticity estimation for bi-elastic film using three separate elasticities in the FEA model. The estimated elasticity of the upper section and lower section are within one standard deviation of the actual elasticity values of 3.6×10^9 Pa and 4.5×10^8 Pa, respectively. The actual elasticity of the mid section is unknown as it is a combination of the upper section elasticity and lower section elasticity.

Table 5.1: Results of elasticity estimation using three elasticity segments

	Homogeneous Flap		Non Homogeneous Flap	
Element	Avg. Estimate	Error	Avg. Estimate	Error
1(Base)	$1.8 \times 10^8 +/- 1.3 \times 10^8$	71.1%	$4.2 \times 10^8 +/- 7.1 \times 10^7$	6.4%
2 (Mid)	$4.4 \times 10^8 +/- 4.3 \times 10^7$	2.2%	$2.1 \times 10^9 +/- 3.5 \times 10^8$	N/A
3(Tip)	$4.9 \times 10^8 +/- 4.8 \times 10^7$	10.2%	$3.3 \times 10^9 +/- 3.1 \times 10^8$	13.8%

The average estimate includes +/- SD taken over 100 filter iterations. The error is computed using the average estimated elasticity and the known elasticity of the flap.

5.4 Discussion

The result for the elasticity estimation of a single elasticity film using a homogeneous elasticity model (**Figure 5.1**) is within 2% of the true solution of 4.5×10^8 Pa. This indicates that the elasticity estimator is well suited for measuring the elasticity of a homogeneous film.

The results for the elasticity estimation of a single elasticity film using three separate elasticities in the FEA model are also in close agreement to the actual elasticity value of 4.5×10^8 Pa, as demonstrated in **Figure 5.6**. The error in the elasticity estimates of the upper, mid and lower sections are 10.2%, 2.2%, 71.1%, respectively. Although there is significant error in the estimated value for the lower section, it is within two standard deviations of the actual value. The standard deviation for the upper, mid and lower sections are 4.8×10^7 Pa, 4.3×10^7 Pa, 1.3×10^9 Pa, respectively. The high level of

error in the estimate of the lower section elasticity can be attributed to the lack of sufficient velocity vectors to provide forcing data. In this case, the flow is primarily in contact with mid section and upper section; therefore, the velocity field at the lower section is sparse.

The elasticity estimates of the bi-elastic film using three separate elasticities in the FEA model are also in close agreement to the actual values of 3.6×10^9 Pa for the tip and 4.5×10^8 Pa for the lower section. The error in the elasticity estimate is 13.8% for the upper section and 6.4% for the lower section. The actual elasticity of the mid section is unknown as it is a combination of the upper section elasticity and mid section elasticity; however, it is expected that it should lie between the estimates for the upper and lower section, this is confirmed in **Figure 5.7**. In this case, the elasticity estimate of the lower section is more accurate; this due to the stiffer elasticity of the upper section. The film deflects less than the previous case; this forces a greater portion of the flow downward and results in a higher vector density than for the previous case. However, the overall vector density is still approximately 20% lower than for the upper and mid section. It only becomes obvious that there exists a high level of discrepancy in the data when considering the standard deviations of the elasticity estimates; in this case, it is clear the standard deviation of the lower section data is significantly higher than for the mid or upper section. A comparison between vector density and error in the estimate is provided in **Figure 5.8**; it is apparent there is a strong correlation between vector density and error (the Pearson correlation is .954). For this particular scenario, it appears that a minimum of 23 velocity vectors along the length of the elasticity segment are required to produce estimates with less than 10% error.

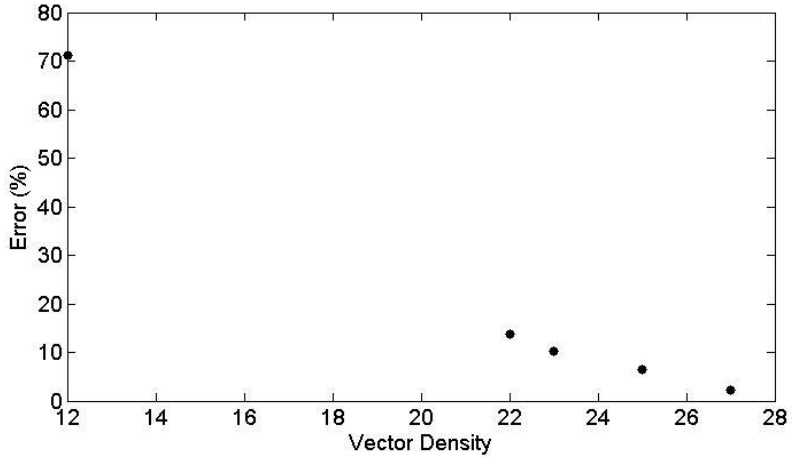

Figure 5.8 Plot of vector density along the length of each elasticity segment versus the error in the average elasticity estimate for that particular segment

Proper selection of *Q*, the elasticity covariance, and the initial guess $\hat{x}$ are required to ensure the stability and repeatability of the estimator routine. It was found that the initial guess must be of the same order of magnitude as the actual elasticity, as evident by the initial guess choice for the non homogeneous case where the actual elasticity is 3.6 $x10^9$ Pa for the tip and 4.5$x10^8$ Pa for the lower section and the corresponding initial guesses are 1 $x10^9$ and 1 $x10^8$. In addition, the covariance of the elasticity for this particular experiment was always an order of magnitude less than the corresponding elasticity. The actual values of *Q* and $\hat{x}$ can be further modified until a fully repeatable estimate is achieved.

5.5 Future Work

Direct *in vivo* application of the outlined elasticity estimation technique will require advancements in intracardiac flow visualization techniques. Current methods,

such as cardiac magnetic resonance (CMR), color ultrasound, or ultrasound PIV, each have limitations in temporal and spatial resolution that must be addressed before this elasticity estimation technique could be applied to *in vivo* data. This is primarily due to the susceptibility of the pressure measurement techniques to dramatically compound even small errors in the velocity data. Improvements in visualization techniques coupled with the design and implementation of filtering techniques [54] to remove noise in the PIV vector field would greatly aid in the future development of a tissue compliance measurement models.

5.5.1 In Vivo Flow Analysis with Ultrasound PIV

This method uses high-frequency sound transmission to track commercially available ultrasound contrast agents (Optison, Definity), or microbubbles, of approximately 4 microns in diameter, that are dispersed within the fluid and serve as flow tracers. By off-line tracking the microbubbles in consecutive frames, a velocity vector field is created. **Figure 5.9** is an illustrative example of echo PIV obtained *in vivo*.

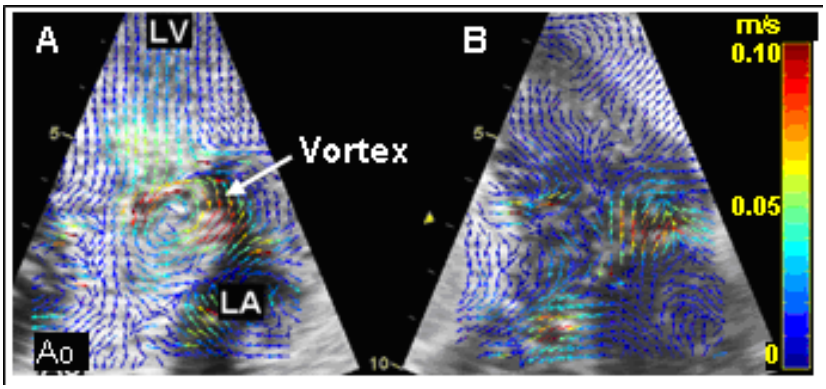

Figure 5.9 Echo PIV vector fields of early filling. A) Baseline. A well formed vortex lasted approximately 30ms. B) Effect of elevated afterload: vortex is disorganized. (Ao, aorta; LA, left atrium)

High temporal resolution of 4 ms [3] is obtainable with an available, clinically used, Vivid 7 ultrasound system. Tracking of particles (microbubbles) can be accomplished by using dedicated DaVis software (La Vision, Inc.) or freeware such as PIVlab [38]. Recent studies validated 2D echo PIV by demonstrating that it generates 2D velocity vectors that closely correlate to those reconstructed from fully 3D optical PIV data ("gold standard") [60, 39]. Multi-plane echo PIV acquisition, (**Figure 10 A**) can be used to provide more complete spatial representation of blood flow velocities when compared to single-plane echo PIV. A rotational device (TomTec) with a fitted transducer (**Figure 10 B**) can be held in a fixed position and rotated in incremental angular steps about a central axis. At each angular plane, several cardiac cycles can be acquired and echo PIV data averaged to reduce measurement noise; the array of 2D scans can then be assimilated to obtain the 3D reconstruction.

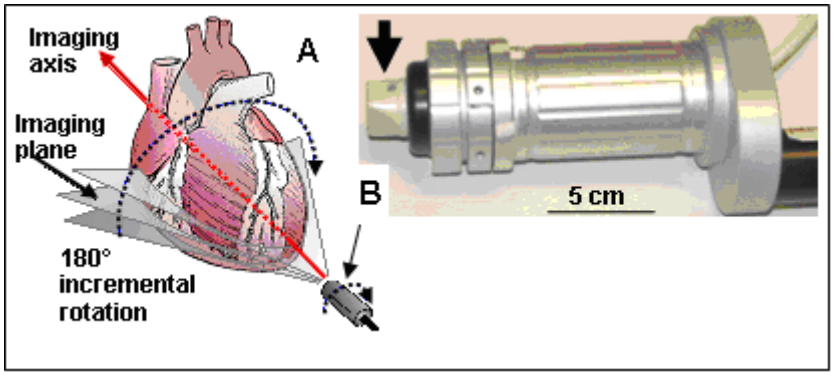

Figure 5.10 A. Multiplane ultrasound acquisition device. **B**, Available (TomTec Life Sciences, Hamden, CT) rotational stepper device fitted with an ultrasound transducer.

Estimation of localized ventricular rigidity, as a diagnosis for hypertrophy, for instance, would likely require a fully 3D reconstruction of the intraventricular flow field. This is due in part to the strongly 3D, turbulent flow encompassing the diastolic vortex (or vortices). Forcing data would likely be especially difficult to obtain given the ensemble size necessary to bring noise in echo-PIV measurements to an acceptable level.

5.5.2 Application to Valvular Physiology

The initial physiological applications of a tissue compliance estimation routine will likely be related to the aortic or mitral valve. Valvular calcification, which leads to stiffening of the leaflets, could be detected without the need for invasive procedures. The boundary conditions of heart valves are more easily defined than the myocardium, and the transmitral (or transaortic) flow is more strongly 2D than the flow field in either the ventricles or atrium. Forcing data can be generated using Doppler ultrasound, which allows for one dimensional in-beam velocity measurements and is often used to the find peak transvalvular velocity when diagnosing valvular stenosis [3]. Another possibility to obtain forcing estimates would be direct measurement of the transvalvular pressure gradient using pressure catheters, this method is reliable but invasive and causes patient discomfort.

As an example of the physiological application of tissue modeling, a brief study is performed using the FEA model outlined in section 5.2.4 to estimate the closure dynamics of the mitral valve. Assuming the elasticity of the mitral valve to be a constant 2090 KPa [61], a distributed, sinusoidal pressure of 13.8 kPa (based on *in vivo* measurements of the transmitral pressure gradient) is applied along the length of the

beam [62]. The thickness of the mitral valve leaflet is assumed to be 1mm and the density is 1.06 g/cc [62], both figures are based on clinical measurements. The simulation results are presented in Figure **5.11**.

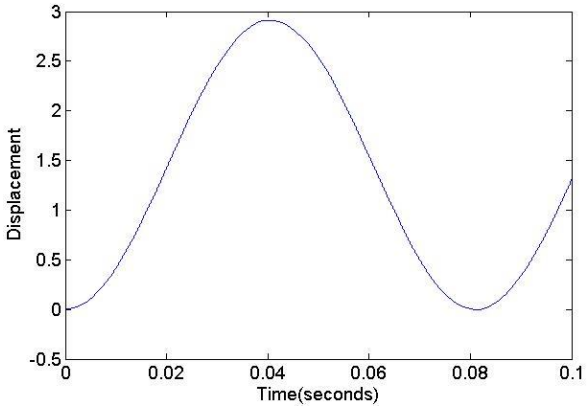

Figure 5.11 Tip displacement vs. time for mitral valve simulation. The valve leaflet is fully open at .0402 s

The valve is found to be fully open at 0.0402 s. Previous *in vivo* studies have shown that the time required for the mitral valve to fully open is 0.04 s with a standard deviation of .01 s, this is based on echocardiogram measurements [63]. This demonstrates that a simplified FEA routine using beam elements can be used to generate a highly accurate FEA analysis of the mitral valve. The deformation of the beam is shown in **Figure 5.12**. It is difficult to make a thorough comparison between the FEA solution and the actual deformation data (obtained from echocardiogram data), primarily because the resting positions are inconsistent and the actual forcing is not a constant. Furthermore, the actual valve utilizes chordae tindineae, small tendons that aid with valve closure, their function is not represented in this model.

The stretch of the valve leaflet was also estimated using the FEA routine. Previous studies investigating leaflet stretching use Sonometric crystals implanted along the length of a porcine heart valve, the position of the crystals can be tracked temporally. Such research has demonstrated that, using a left heart model, stretching along the central portion of the mitral valve leaflet during systole may approach 1.5 times the unstretched length [64]. Using the simplified FEA hermetian beam simulation, leaflet length is shown to stretch by a factor of 2.5. The discrepancy between the results is likely due to the oversimplified geometry of the FEA simulation; as previously mentioned, only a beam like structure is simulated and the effects of the full leaflet and chordae are disregarded.

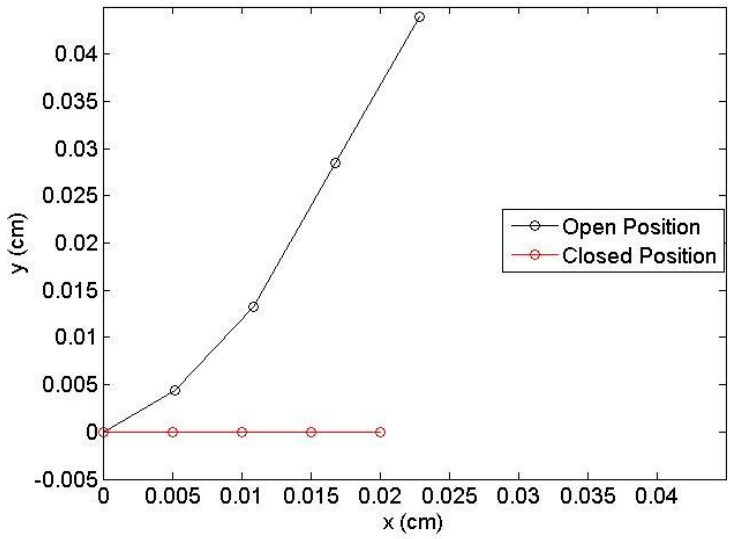

Figure 5.12. Deformation of beam using FEA mitral valve simulation.

True estimates for the mitral valve elasticity, for example, may be impossible to derive without invasive techniques such as direct measurement of transvalvular pressures with a catheter. However, estimates for localized changes in elasticity, based on localized forcing data as derived from ultrasound PIV, could offer incite into early stages of valve calcification or other stiffening and degradation conditions. Despite their limitations, simplified models such as the FEA routine used to model a leaflet could be used as a clinical diagnostic method. Performing a comprehensive FEA simulation of the ventricle would be extremely difficult in a clinical setting. Thus, it is up to the researcher to develop simplified techniques that can be implemented clinically, but have been verified through rigorous experimentation.

5.6 Conclusion

An elasticity estimation process is developed that utilizes forcing data derived from optical-PIV to measure the elasticity of a thin, cellulose acetate film. Three distinct subroutines are required for elasticity estimation: (1) velocity field acquisition via optical-PIV (2) solving Poisson's equation to determine pressure, and (3) using an ensemble Kalman filter coupled with an FEA program to derive the elasticity. The estimation process in applied to films of both homogeneous and non homogeneous elasticity and elasticity values along the length are determined.

The results show that it is possible to estimate the elasticity of a thin film based on PIV velocity fields and displacement measurements. In addition, it is possible to accurately determine the elasticity

Chapter 6

CONCLUSIONS AND FUTURE WORK

This dissertation represents a culmination of my research on PIV techniques related to the study of intracardiac flow. When compared to various existing modeling and visualization methods that are being used by researchers, ultrasound based methods offer clear benefits: they are inexpensive and data can be acquired in almost any clinical setting; temporal resolution exceeds that of other *in vivo* techniques, performing scans is noninvasive and results in little patient discomfort; finally, data can be processed offline using techniques like PIV. Three separate studies are presented that demonstrate the importance of ultrasound PIV as a visualization tool: the accuracy of the ultrasound PIV method is demonstrated in Chapter 3, a novel multi-plane ultrasound PIV system is implemented in Chapter 4 to resolve LV flow, and Chapter 5 introduces a modeling technique that estimates cardiac tissue compliance using data derived from PIV.

In Chapter 3 it is demonstrated that 2D velocity vector fields obtained by a clinically available, portable ultrasound machine coupled with DaVis PIV processing software correlate closely with those generated by optical-PIV, a technique well established as a "gold standard" for flow visualization. The vortex ring imaged in this study, which was dimensionally similar to the diastolic vortex, contained a significant out-of-plane component; much of the measurement error is shown to occur from the inability of 2D ultrasound to measure out-of-plane flow motion. Additional measurement error can be attributed to distortion due to the scan conversion process of ultrasound data. Given a sufficiently high ultrasound frame rate, a time filter can be applied to minimize noisy data. Thus, ultrasound-PIV is precise and accurate in the measured velocity range

with most limitations related to 2D scanning of flow, which naturally contains velocity vectors in multiple directions [39].

The study performed in Chapter 4 utilizes a multi-plane ultrasound PIV system to resolve the left intraventricular flow in a heart model. The results strongly suggest that angular positioning of the mechanical mitral valve is an important determinant of intracardiac hemodynamic conditions. Furthermore, it is demonstrated that a comprehensive understanding of LV dynamics is necessary to fully quantify mitral valve performance. The LV flow is complex and strongly three-dimensional; thus, studying the left intraventricular flow using two dimensional imaging techniques can lead to inaccurate findings. This study demonstrates that using a single two dimensional plane to quantify MHV performance is unacceptable and can lead to misleading conclusions about the preferred positioning of an MHV. Imaging techniques such as multi-plane PIV can be used to mitigate this problem.

In Chapter 4, an elasticity estimation process is developed that utilizes forcing data derived from optical-PIV to measure the elasticity of a thin, cellulose acetate film. Three distinct subroutines are required for elasticity estimation: (1) velocity field acquisition via optical-PIV (2) solving Poisson's equation to determine pressure, and (3) using an ensemble Kalman filter coupled with an FEA program to derive the elasticity. The estimation process in applied to films of both homogeneous and non homogeneous elasticity and elasticity values along the length are determined. The results show that it is possible to estimate the elasticity of a thin film based on PIV velocity fields and displacement measurements. In addition, it is possible to accurately determine the elasticity of films with non-homogeneous elasticity. Considering the success of this

technique using optical-PIV, it should also be possible to estimate elasticity based on echo-PIV data, which is a future direction of my research.

Existing work that establishes a basis for ultrasound PIV [7 ,8] focused on the development of the technique based on comparisons with know solutions and qualitatitative alanysis of complex flows, this work advances technical knowledge by specifically quantifying the ability of ultrasound PIV to analyze intracardiac hemodynamics. This establishes a basis for clinical use of ultrasound PIV, particularly in the context of ventricular hemodynamics. Furthermore, the development of a novel tissue compliance diagnostic technique in Chapter 5 demonstrates how researchers could utilize the ultrasound PIV technique for in vivo, clinical measurements.

6.1 Summary of Future Work

With the creation of improved ultrasound systems, particularly those that allow for three dimensional imaging with high spatial and temporal resolution, it will likely be possible to fully quantify the LV flow. This could allow for precise measurements of cardiac efficiency and also detailed analysis of the effects of MHVs, pacemakers, and other cardiac dysfunctions. Additionally, a better understanding of the interactions between blood flow and heart walls is also necessary to quantify MHV performance. The effects of tissue-flow interactions remain mostly unknown; yet, this knowledge is vital to the creation of improved replacement heart valves. Innovation in this field will require models that precisely replicate the intricate boundary conditions of the myocardium.

Perhaps the most important direction of future work is on the creation of early diagnostic techniques that are immediately viable in a clinical setting. Although ultrasound PIV has high temporal and spatial resolution, the measurements are noisy and

can be difficult to interpret. It is important that researchers continue to search for parameters and techniques that can be readily extrapolated from visualization methods. The advents of improved data filtering techniques for ultrasound or the study of the diastolic vortex as a measure for cardiac health are two examples.

My future work will include the creation of devices that allow for more precise multi-plane ultrasound data acquisition. This will involve the development of servo controlled holders for the ultrasound transducers so that the 2D imaging plane can sweep laterally and rotate to fully image a particular region. This will require data processing routines that can convert multiple 2D planes into a unified 3D model. The result of this work will be the creation of a 3D imaging technique that can easily and inexpensively be performed in a clinical setting. Ultrasound equipment is used extensively in clinical settings, thus only the transducer controller and data processing software would be required. Additional future work involves the improvement of existing techniques used by clinicians for the diagnosis of aortic and mitral stenosis, an example being extensive study of contrast enhanced Doppler. I will also focus on creating new estimates for valve leakage and leaflet openness, parameters that can be difficult to assess.

REFERENCES

1. The Top 10 Causes of Death. World Health Organization. May, 2014 http://www.who.int/mediacentre/factsheets/fs310/en/

2. Ganong WF. Review of Medical Physiology, 22nd Edition. Lange Medical Books/McGraw Hill. 2005. 547-576.

3. Sengupta P, et al. Emerging Trends in CV Flow Visualization. JACC Cardiovasc Imaging. 2012 Mar;5(3):305-16

4. Gharib M, Kremers D, Koochesfahani MM, Kemp M. Leonardo's vision of flow visualization Experiments in Fluids 33 (2002) 219–223

5. Pohost G. The History of Cardiovascular Magnetic Resonance J Am Coll Cardiol Img. 2008;1(5):672-678

6. Borazjan I, Westerdale J, et al. Left Ventricular Flow Analysis: Recent Advances in Numerical Methods and Applications in Cardiac Ultrasound Comput Math Methods Med 2013 17;2013:395081

7. Kim HB, Hertzberg J and Shandas R Development and validation of echo-PIV Exp. Fluids 2004 36: 455–462.

8. Liu L, Zheng H, Williams L, et al. Development of a custom-designed echo particle image velocimetry system for multi-component hemodynamic measurements: system characterization and initial experimental results. Phys Med Biol 2008; 53:1397-1412.

9. Hong G-R, Pedrizzetti G, Tonti G, et al. Characterization and quantification of vortex flow in the human left ventricle by contrast echocardiography using vector particle image velocimetry. J Am Coll Cardiol Img 2008; 1:705-717.

10. Sengupta PP, Khandheria BK, Korinek J, et al. Left ventricular isovolumic flow sequence during sinus and paced rhythms: new insights from use of high-resolution Doppler and ultrasonic digital particle imaging velocimetry. J Am Coll Cardiol 2007; 49:899-908.

11. Fei R, Merzkirch W Investigations of the measurement accuracy of stereo particle image Velocimetry. Exp in Fluids 2004; 37:559-565.

12. Keane R D, Adrian R J Optimization of particle image velocimeters: I. Double pulsed systems Meas. Sci.Technol 1990; 1:1202–1215.

13. Cooke J, Hertzberg J, Boardman M, Shandas R. Characterizing vortex ring behavior during ventricular filling with Doppler echocardiography: an in vitro study. Ann Biomed Eng 2004; 32:245-256.

14. Bland JM, Altman DG. Statistical methods for assessing agreement between two methods of clinical measurement. Lancet, i, 1986; 307-310.

15. Moore D. Basic Practice of Statistics (4th Edition). WH Freeman Company, New York, NY; 2006

16. Jiamsripong P, Calleja AM, Alharthi MS, et al. Impact of acute moderate elevation in left ventricular afterload on diastolic transmitral flow efficiency: analysis by vortex formation time. J Am Soc Echocardiogr 2009; 22:427-431.

17. Sengupta PP, Krishnamoorthy VK, Korinek J, et al. Left ventricular form and function revisited: applied translational science to cardiovascular ultrasound imaging. J Am Soc Echocardiogr. 2007; 20:539-551.

18. Gharib M, Rambod E, Kheradvar A, Sahn DJ, Dabiri JO. Optimal vortex formation as an index of cardiac health. Proc Natl Acad Sci. 2006; 103:6305-6308.

19. Appleton CP, Hatle LK, Popp RL. Relation of transmitral flow velocity patterns to left ventricular diastolic function: new insights from a combined hemodynamic and Doppler echocardiographic study. J Am Coll Cardiol 1988; 12:426-440.

20. Appleton CP, Jensen JL, Hatle LK, Oh JK. Doppler evaluation of left and right ventricular diastolic function: a technical guide for obtaining optimal flow velocity recordings. J Am Soc Echocardiogr 1997; 10:271-292.

21. Jacobsen J, Adeler, P, Kim W, Houlind K, Pedersen E, Larsen J. Evaluation of a 2D Model of the Left Side of the Human Heart against Magnetic Resonance Velocity Mapping. Cardiovascular Eng 2001; 1:59-76.

22. Garcia D, Del Alamo J, Tanne D, et al. Two-dimensional intraventricular flow mapping by digital processing conventional color-Doppler echocardiography images. IEEE Trans Med Imaging 2010

23. Kilner PJ, Yang GZ, Wilkes AJ, Mohiaddin RH, Firmin DN, Yacoub MH. Asymmetric redirection of flow through the heart. Nature 2000; 404:759-761.

24. Kim WY, Walker PG, Pedersen EM, et al. Left ventricular blood flow patterns in normal subjects: a quantitative analysis by three-dimensional magnetic resonance velocity mapping. J Am Coll Cardiol 1995 26:224-238.

25. Kim HB, Hertzberg J, Lanning C, Shandas R Noninvasive measurement of steady and pulsating velocity profiles and shear rates in arteries using echo-PIV: in vitro validation studies. Ann Biomed Eng 2004 32:1067-1076.

26. Gharib M, Rambod E, Kheradvar A, Sahn DJ, Dabiri JO. Optimal vortex formation as an index of cardiac health. Proc Natl Acad Sci U S A 2006;103:6305-8

27. Sengupta PP, Korinek J, Belohlavek M, et al. Left ventricular structure and function: basic science for cardiac imaging. J Am Coll Cardiol 2006; 48:1988-2001.

28. Jiamsripong P, Calleja AM, Alharthi MS, et al. Increase in the late diastolic filling force is associated with impaired transmitral flow efficiency in acute moderate elevation of left ventricular afterload. J Ultrasound Med 2009; 28:175-182.
29. Mukdadi OM, Kim HB, Hertzberg J, Shandas R. Numerical modeling of microbubble backscatter to optimize ultrasound particle image velocimetry imaging: initial studies. Ultrasonics 2004;42:1111-1121.

30. Borazjani I, Sotiropoulos F. The Effect of Implantation Orientation of a Bileaflet Mechanical Heart Valve on Kinematics and Hemodynamics on an Anatomic Aorta. J Biomech Eng. 2010; 132(11)

31. Faludi R. et al. Left ventricular flow patterns in healthy subjects and patients with prosthetic mitral valves: An in vivo study using echocardiographic particle image velocimetry. J Thorac Cardiovasc Surg. 2010; 139(6):1501-10

32. Lim WL, Chew YT, Chew TC, Low HT. Steady flow dynamics of prosthetic aortic heart valves: a comparative evaluation with PIV techniques. J Biochem 1998; 32: 411-421.

33. Rahimtoola, S. H. Choice of prosthetic heart valve for adult patients. J Am Coll Cardiol. 2003; 41: 893–904.

34. Rahimtoola, S. H. Choice of prosthetic heart valve for adult patients – an update. J Am Coll Cardiol. 2010; 55:2413–26

35. Sengupta P, Burke R, Khandheria B, Belohlavek M. Following the Flow in Chambers. Heart Failure Clin. (2008)

36. Akutsu T, Masuda T, Three-dimensional flow analysis of a mechanical bileaflet mitral prosthesis. J Artif Organs. 2003; 6:112-123

37. Akutsu T, Saito J. Dynamic particle image velocimetry flow analysis of the flow field immediately downstream of bileaflet mechanical mitral prostheses. J Artif Organs. 2006; 9:165-178

38. Thielicke, W. and Stamhuis, E. J. (2014): PIVlab - Time-Resolved Digital Particle Image Velocimetry Tool for MATLAB (version: 1.35), http://pivlab.blogspot.com/ (accessed on 12/16/2015)

39. Westerdale J, Belohlavek M, McMahon E, Jiamsripong P, Heys JJ, Milano M, "Flow Velocity Vector Fields by Ultrasound Particle Imaging Velocimetry: In Vitro Comparison to Optical Flow Velocimetry." J Ultrasound Med. 2011; 30(2):187-95

40. Kim HB, Hertzberg JR, Shandas R. Echo PIV for flow field measurements in vivo. Biomed Sci Instrum. 2004; 40:357-63

41. Leverett LB, Hellums JD, Alfrey CP, Lynch EC. Red Blood Cell Damage by Shear Stress. Biophys J. 12 1972; 257-273

42. Fraser KH, Zhang T, Taskin ME, Griffith BP, Wu ZJ. A quantitative comparison of mechanical blood damage parameters in rotary ventricular assist devices: shear stress, exposure time and hemolysis index. J Biomech Eng. 2012 Aug;134(8):081002

43. Stijnen JMA, van de Vosse FN, Baaijens FTP. Influence of Prosthetic Mitral Valve Orientation of Left Ventricular Flow. Comput Cardiol 2001

44. Machler H, Perthel M, Reiter G, Reiter U, Zink M, Bergmann P, Waltensdorfer A, Laas J. Influence of bileaflet prosthetic mitral valve orientation on left ventricular flow – an experimental in vivo magnetic resonance imaging study. Euro J Cardiothorac Surg. 2004; 26:747-753

45. Machler H, Reiter G, Perthel M, Reiter U, Bergman P, Zink M, Rienmuller R, Laas J. Influence of a tilting prosthetic mitral valve orientation on the left ventricular flow – an experimental in vivo magnetic resonance imaging study. Euro J Cardiothorac Surg. 2007; 32:102-107

46. Martínez-Legazpi P, Bermejo J, Benito Y, Yotti R, Pérez Del Villar C, González-Mansilla A, Barrio A, Villacorta E, Sánchez PL, Fernández-Avilés F, del Álamo JC. Contribution of the diastolic vortex ring to left ventricular filling. J Am Coll Cardiol. 2014; 64(16):1711-21.

47. Sengupta PP, Khandheria BK, Korinek J. et al. Left ventricular isovolumic flow sequence during sinus and paced rhythms: new insights from use of high-

resolution Doppler and ultrasonic digital particle imaging velocimetry, J Am Coll Cardiol, 49(8) (2007) 899-908

48. Barber J, Kaspera F, Ratliff NB, et al. Mechanical properties of myxomatous mitral valves. J Thorac Cardiovasc Surg. 122 (2001) 955-962

49. Krishnamurthy G, Ennis DB, Itoh A, et al, Material properties of the ovine mitral valve anterior leaflet in vivo from inverse finite element analysis, Am J Physiol Heart Circ Physiol. 295 (2008) 1141-1149

50. Shandas R, Gharib M, Liepman D, Shiota T, Sahn DJ, Experimental studies to define the geometry of the flow convergence region. Laser Doppler particle tracking and color Doppler imaging. Echocardiography, 9(1) (1992) 43-50

51. Grande-Allen KJ, Barber JE, Klatka KM, Houghtaling PL, Vesely I, Moravec CS, McCarthy PM, Mitral valve stiffening in end-stage heart failure: evidence of an organic contribution to functional mitral regurgitation. J Thorac Cardiovasc Surg, 130 (2005) 783–790

52. Chen L, Yin FC, May-Newman K. The structure and mechanical properties of the mitral valve leaflet-strut chordae transition zone. J Biomech Eng, 126 (2004) 244–251

53. Gurka R, Liberzon A, Hefetz D, Rubinstein D, Shavit U, Computation of pressure distribution using PIV velocity data, Proc. Int. Workshop on PIV'99 (1999) 671–76

54. Charonko J, King C, Smith B, Vlachos P. Assessment of pressure field calculations from particle image velocimetry measurements. Meas. Sci. Technol 21 (2010)

55. van Oudheusden BW, Scarano F, Roosenboom EWM, Casimiri EWF, Souverein LJ. Evaluation of internal forces and pressure fields from lanar velocimetry data for incompressible and compressible flows. Exp Fluids (2007) 43:153-162

56. Driscoll TA, A MATLAB Toolbox for Schwarz-Christoffel mapping. ACM Trans. Math. Soft. 22 (1996) 168-186.

57. Aldraihem OJ, Wetherhold RC, Singh T, Distributed Control of Laminated Beams: Timoshenko Theory vs. Euler-Bernoulli Theory, J Intell Mater Syst Struct 8 (1997) 149-57

58. Kwon Y, Bang H. The finite element method using MATLAB, 2nd ed., CRC Press, Boca Raton, FL, 2000

59. Gillijns S, Barrero Mendoza O, Chandrasekar J, De Moor BLR, Bernstein DS, Ridley A. "What is the Ensemble Kalman Filter, and How well Does It work?" ACS Proceedings, Minneapolis (MN), USA, 2006

60. Simon D, "Optimal State Estimation", Wiley and Sons 2006

61. Wei F, Westerdale J, McMahon EM, Belohlavek M, Heys JJ. Weighted least-squares finite element method for cardiac blood flow simulation with echocardiographic data. Comput Math Methods Med 2012;2012:371315.

62. Cochran RP, and Kunzelman KS, "Effect of Papillary Muscle Position on Mitral Valve Function: Relationship to Homografts", Ann Thorac Surg 66: S155-S161, 1998.

63. Hammer P, Perrin D, Nido P, Howe R, Image-based mass-spring model of mitral valve closure for surgical planning. Proc. of SPIE Medical Imaging: Visualization, Image-guided Procedures, and Modeling, vol. 6918, 69180Q, 2008.

64. Masanori N, Wada S, Yamaguchi T. Influence of the Opening Mode of the Mitral Valve Orifice on Intraventricular Hemodynamics, Annals of Biomedical Engineering 2006

65. Gao B. Mitral valve mechanism under diseased and repair condition. (Doctoral Dissertation) Retrieved from Texas Digital Library. Texas Tech Univ. 2012

APPENDIX A

COPYRIGHT

Chapter 3 is reproduced with permission from Westerdale J, Belohlavek M, McMahon E, Jiamsripong P, Heys JJ, Milano M, “Flow Velocity Vector Fields by Ultrasound Particle Imaging Velocimetry: In Vitro Comparison to Optical Flow Velocimetry.” J Ultrasound Med. 2011; 30(2):187-95